University of Minho
School of Sciencies

Edgar Barros Sousa

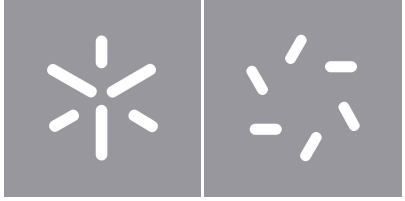
Pulsed-Laser Fabrication of Gold Plasmonic Nanoparticles in Thin Films for LSPR Sensing Applications

october 2025

Pulsed-Laser Fabrication of Gold Plasmonic Nanoparticles in Thin Films for LSPR Sensing Applications

Edgar Sousa

UMinho | 2025



University of Minho
School of Sciences

Edgar Barros Sousa

Pulsed-Laser Fabrication of Gold Plasmonic Nanoparticles in Thin Films for LSPR Sensing Applications

Master's Dissertation

Master's in Physics
Dissertation supervised by
Doctor Michael Scott Belsley
Doctor Joel Pinto Borges

october 2025

Copyright and Terms of Use for Third Party Work

This dissertation reports on academic work that can be used by third parties as long as the internationally accepted standards and good practices are respected concerning copyright and related rights.

This work can thereafter be used under the terms established in the license below.

Readers needing authorization conditions not provided for in the indicated licensing should contact the author through the RepositóriUM of the University of Minho.

License granted to users of this work:



CC BY

https://creativecommons.org/licenses/by/4.0/

Agradecimentos

Quero agradecer e dedicar este trabalho a dois grandes pilares, ao vô Milinho e ao vô João, que sei com certeza que estariam orgulhosos de o ver concluído. Não menos importantes, agradeço aos meus pais, irmã, avós e restante família que me ajudaram a tornar no homem que sou hoje.

Um agradecimento especial à minha namorada Joana por todo o carinho, apoio e compreensão, e também a todos os amigos que me acompanharam nos bons e maus momentos destes anos inesquecíveis. Sem a vossa presença já teria desistido.

Agradeço aos meus orientadores, o professor Michael Belsley e o doutor Joel Borges, pela confiança depositada em mim e por toda a ajuda neste enigmático trabalho. Não posso também deixar de agradecer aos restantes professores que marcaram o meu percurso académico.

Um grande obrigado ao futuro doutor Nelssom Cunha, pois sem ele o laboratório de ótica ultrarrápida estaria parado, e ao professor José Gomes pela motivação para estudar ótica.

Agradeço também ao Centro de Física (CF-UM-UP) e à Fundação para a Ciência e a Tecnologia (FCT) pela bolsa de investigação associada ao projeto 20/ECUM/CFUM/2024 – PlasPolML.

Em último lugar, mas não menos importantes, agradeço aos funcionários do bar do CP1, pois sem merendar não se pode trabalhar.

Statement of Integrity

I hereby declare having conducted this academic work with integrity.

I confirm that I have not used plagiarism or any form of undue use of information or falsification of results along the process leading to its elaboration.

I further declare that I have fully acknowledged the Code of Ethical Conduct of the University of Minho.

University of Minho, Braga, october 2025

Assinado por: **Edgar Barros Sousa**
Num. de Identificação: 30560576
Data: 2025.10.31 18:47:30+00'00'

Edgar Barros Sousa

Abstract

We demonstrate a controlled method for forming plasmonic gold nanoparticles in ZnO thin films using pulsed laser annealing with real-time optical monitoring. Gold nanoparticles with an average radius of 3 nm were initially embedded in sputtered ZnO films on fused silica substrates. Using 532 nm pulses from a Q-switched Nd:YAG laser (20 - 40 mJ, 10 Hz), we induced controlled annealing while simultaneously monitoring transmission spectra via an in-situ broadband spectrometer. After about 10 to 100 laser pulses, depending on the location on the sample's surface, a plasmonic resonance dip emerged at approximately 550 nm, deepening and broadening with continued exposure. The process stabilized after 300 to 400 shots, producing larger nanoparticles (20 - 200 nm diameter) partially protruding from the ZnO surface. SEM analysis confirmed significant particle coarsening and migration toward the film surface. Numerical simulations were developed to correlate the observed spectral evolution with nanoparticle size and embedding depth, and a complementary temperature model indicated that local heating during laser irradiation can reach values sufficient to promote melting and coalescence. This approach demonstrates effective control over plasmonic nanostructure formation for sensing applications, providing advantages over conventional thermal annealing through spatial selectivity, rapid processing and real-time process monitoring.

Keywords Pulsed laser annealing, LSPR, Plasmonic nanoparticles, Gold nanoparticles, Spectrometry, Nanocomposite thin films

Resumo

Demonstramos um método para formar nanopartículas de ouro plasmónicas, de forma controlada, em filmes finos de ZnO, utilizando recozimento induzido por um laser pulsado, com monitorização ótica em tempo real. Nanopartículas de ouro com um tamanho médio inicial de 6 nm foram inicialmente incorporadas em filmes de ZnO pulverizados em substratos de sílica fundida. Utilizando pulsos com 532 nm de um laser Nd:YAG Q-switched (20 - 40 mJ, 10 Hz), induzimos um recozimento controlado enquanto monitorizávamos simultaneamente os espectros de transmissão com um espectrómetro de banda larga in situ. Após cerca de 10 a 100 pulsos do laser, dependendo da localização na superfície da amostra, surgiu um vale de ressonância plasmónica a aproximadamente 550 nm, aprofundando-se e alargando-se com a exposição contínua. O processo estabilizou após 300 a 400 disparos, produzindo nanopartículas maiores (20 - 200 nm de diâmetro) que se projetavam parcialmente da superfície de ZnO. A análise com MEV confirmou um aumento significativo do tamanho das partículas e a sua migração em direção à superfície do filme. Simulações numéricas foram desenvolvidas para correlacionar a evolução espectral observada com o tamanho das nanopartículas e a profundidade de incorporação, e um modelo de temperatura complementar indicou que o aquecimento local durante a irradiação a laser pode atingir valores suficientes para promover a fusão e a coalescência. Esta abordagem demonstra um controlo eficaz sobre a formação de nanoestruturas plasmónicas para aplicações de deteção, oferecendo vantagens face ao recozimento térmico convencional devido à seletividade espacial, processamento rápido e monitorização do processo em tempo real.

Palavras-chave Recozimento com laser pulsado, LSPR, Nanopartículas plasmónicas, Nanopartículas de ouro, Espetrometria, Filmes finos nanocompósitos

Contents

1 Introduction **2**

1.1 Introduction and objectives . . . 2

1.2 Thesis structure . . . 3

2 Nanoparticle plasmonics **4**

2.1 Surface Plasmon Polaritons . . . 5

2.2 Localized Surface Plasmon Resonance . . . 6

2.2.1 Quasistatic approximation . . . 6

2.2.2 Mie theory . . . 8

2.3 Calculation of extinction efficiencies for case examples . . . 9

3 Self-assembly of nanoparticles **13**

3.1 Thermal annealing . . . 13

3.2 Laser annealing . . . 14

4 Experimental methods **16**

4.1 Sample preparation . . . 16

4.2 Laser annealing setup . . . 17

4.3 In-situ real-time optical monitoring . . . 18

4.4 SEM characterization . . . 20

5 Results and discussion **21**

5.1 Thermal annealing data . . . 21

5.1.1 Spectrometry . . . 21

5.1.2 Nano-morphology . . . 22

5.2 In-situ spectrometry . . . 23

5.3 Morphological analysis . . . 28

5.4 Numerical modeling 34

6 Conclusions **37**

List of Figures

1 Schematic of an SPP propagating along a metal–dielectric interface, showing the electric and magnetic field components, surface charge oscillations, and evanescent field decay with penetration depths δ_1 and δ_2. Reproduced from [16]. 6

2 Schematic of a localized surface plasmon resonance (LSPR) in a metallic nanoparticle, showing the displacement of the electron cloud by the oscillating electric field of the incident light. Reproduced from [18]. 7

3 Schematic of a metallic spherical nanoparticle embedded in a dielectric medium under a constant external electric field E_0 applied along the z axis. 7

4 Comparison of the extinction cross sections (σ_{ext}) for a spherical gold nanoparticle ($R = 10\,\text{nm}$) and an ellipsoidal gold nanoparticle ($a = 5\,\text{nm}$, $b = 10\,\text{nm}$, $c = 15\,\text{nm}$) in a dielectric medium with permittivity $\varepsilon = 3$. The spectra are shown for light polarized along each principal axis, highlighting the splitting of the plasmon resonance due to shape anisotropy. Simulated using the MNPBEM software [23]. 10

5 Extinction efficiency ($Q_{\text{ext}} = \frac{\sigma_{ext}}{\pi R^2}$) of a spherical gold nanoparticle embedded in ZnO [24], shown for different particle radii, highlighting the shifting of the plasmon resonance due to change in size. Simulated using the MNPBEM software [23]. 11

6 Extinction efficiency ($Q_{\text{ext}} = \frac{\sigma_{ext}}{\pi R^2}$) of a spherical gold nanoparticle with radius $R = 25\,\text{nm}$, shown for different medium electric permittivities, highlighting the shifting of the plasmon resonance due to change in medium permittivity. Simulated using the MNPBEM software [23]. 12

7 Experimental setup for the laser annealing process, showing the laser source, fluence tuning optics, sample stage, and monitoring system. 17

8 Emission spectrum of the Thorlabs MNWHL4 white light LED. Reproduced from [32] . . 19

9 Emission spectrum of the "sun-like" LED. 19

10 Transmittance spectra of the thermally annealed Au-ZnO thin films comparing the treatments at different temperatures with the as-deposited film. 22
11 Transmittance spectrum of the Au-ZnO thin film treated at $800\,^{\circ}$C showing the central wavelength of the LSP resonance and the boundaries of the FWHM. 22
12 SEM micrograph of thermally annealed Au–ZnO thin film at $800\,^{\circ}$C. 23
13 Size distribution histogram of Au NPs corresponding to the SEM image in Fig. 12. 23
14 Transmittance spectra of the Au–ZnO thin films treated at $160\,$mW recorded at successive irradiation times, illustrating the evolution of the LSPR dip position, depth, and FWHM for different number of applied pulses. a) 15 pulses; b) 75 pulses, c) 268 pulses and d) 451 pulses. 25
15 Transmittance spectra of the Au–ZnO thin films treated at $190\,$mW recorded at successive irradiation times, illustrating the evolution of the LSPR dip position, depth, and FWHM for different number of applied pulses. a) 9 pulses; b) 71 pulses, c) 152 pulses and d) 438 pulses. 26
16 Transmittance spectra of the Au–ZnO thin films treated at $220\,$mW recorded at successive irradiation times, illustrating the evolution of the LSPR dip position, depth, and FWHM for different number of applied pulses. a) 9 pulses; b) 50 pulses, c) 88 pulses and d) 299 pulses. 27
17 Transmittance spectra of the Au–ZnO thin films after laser annealing with approximately 500 pulses at different laser powers compared to the spectra of the as-depostied and the thermally annealed at $800\,^{\circ}$C samples. 28
18 Morphological characterization of the Au–ZnO thin film treated at $160\,$mW. a) SEM micrographs for different laser powers and b) corresponding nanoparticle size distribution. 30
19 Morphological characterization of the Au–ZnO thin film treated at $190\,$mW. a) SEM micrographs for different laser powers and b) corresponding nanoparticle size distribution. 31
20 Morphological characterization of the Au–ZnO thin film treated at $220\,$mW. a) SEM micrographs for different laser powers and b) corresponding nanoparticle size distribution. 32
21 Morphological characterization of the Au–ZnO thin film treated at $250\,$mW. a) SEM micrographs for different laser powers and b) corresponding nanoparticle size distribution. 33
22 Normalized extinction efficiency ($Q_{\text{ext}} = \frac{\sigma_{ext}}{\pi R^2}$) of a spherical gold nanoparticle with radius $R = 70\,$nm, compared in the air and in ZnO thin film. Simulated using the MNPBEM software [23]. 35

23 Normalized extinction efficiency ($Q_{\text{ext}} = \frac{\sigma_{ext}}{\pi R^2}$) of a spherical gold nanoparticle with radius $R = 70\,\text{nm}$, for different values of fraction of shell volume. Simulated using the STRATIFY software [35]. 35

24 Temporal evolution of the temperature of a spherical gold nanoparticle with radius $R = 70\,\text{nm}$, under a $10\,\text{ns}$ laser pulse with $F = 200\,\text{mJ/cm}^2$ embbeded in a ZnO film or in air. 36

List of Tables

1 Optical parameters of the LSPR dip for different laser powers and for the thermally annealed sample. Associated with Fig. 17. 28
2 Nanoparticle counts, average nanoparticle radius, standard deviation, and estimated surface coverage obtained from SEM image analysis of the sample treated at $160\,\mathrm{mW}$. . 30
3 Nanoparticle counts, average nanoparticle radius, standard deviation, and estimated surface coverage obtained from SEM image analysis of the sample treated at $190\,\mathrm{mW}$. . 31
4 Nanoparticle counts, average nanoparticle radius, standard deviation, and estimated surface coverage obtained from SEM image analysis of the sample treated at $220\,\mathrm{mW}$. . 32
5 Nanoparticle counts, average nanoparticle radius, standard deviation, and estimated surface coverage obtained from SEM image analysis of the sample treated at $250\,\mathrm{mW}$. . 33

"Habrían creído a sus obras y no a sus palabras, porque las palabras no sirven para apoyar las obras, sino que las obras se bastan."

— Miguel de Unamuno, San Manuel Bueno, mártir

Chapter 1

Introduction

1.1 Introduction and objectives

Plasmonic nanomaterials are recognized by the scientific community as powerful transducer platforms for developing molecular sensors, also offering the possibility to explore strong near-field and quantum effects. Nevertheless, few nanodevices have reached the market, despite many related publications [1]. Nanomaterials based on noble metal nanoparticles (e.g. gold and/or silver nanoparticles) appear among the most popular since they show remarkable optical responses to incident electromagnetic fields owing to localized surface plasmon resonances (LSPRs) in the visible range. Plasmonic NPs are employed for sensing because their LSPRs are affected by subtle changes in the refractive index (RI) of the environment. Therefore, the latter can cause a spectral shift of the LSPR band peak or a slight change of its shape, which can be detected by transmittance LSPR spectroscopy [2].

Among different techniques to develop plasmonic sensors, a physical vapour deposition technique such as sputtering can be a cost-effective and environmentally-sound technology to attain this objective. Nevertheless, a post-deposition treatment might be required to obtain noble metal nanoparticles with sufficient sizes, and thermal annealing is a popular approach to induce the self-assembly of the nanoparticles [3].

As demonstrated in the literature, one-step reactive DC magnetron sputtering deposition allows the formation of noble metal clusters only with sizes up to 10 nm [4], which are grown throughout a host matrix. The host matrix (usually an oxide [5–7]) confers robustness to the nanocomposite material, however it may constrain the mobility and diffusion of gold atoms during their self-assembly, depending on the selected oxide. This experimental procedure does not allow the development of noble metal nanoparticles with controlled sizes, shapes and distributions. Therefore, even if it is demonstrated that this kind of plasmonic thin films (when properly functionalized) manifest good sensitivities being able to detect a particular gas [6] or a molecule [8], the figure of merit of these sensors (defined as the sensitivity divided by the LSPR

band width, $S/\Delta\lambda$ [9]) could be improved if the size distribution of the nanoparticles is narrower.

In this regard, there are studies in literature that demonstrate the use of short-pulse laser beams, within the resonance band, to enable the self-assembly of nanoparticles in narrow and short-range distributions [10]. Considering the limitations and advantages of these two different self-assembly approaches (thermal annealing vs. laser annealing), the main objective of this work was the development of a controlled laser annealing system with real-time spectroscopic feedback, as a potential alternative to standard procedure of thermal treatment at high temperatures. To perform the tests with the laser annealing system, ZnO thin film was chosen as the host matrix, mainly due to its antimicrobial properties that might be relevant for application in particular environments [11].

1.2 Thesis structure

Having presented a brief state of the art and the main objectives of this work, we proceed in Chapter 2 to introduce the theoretical framework underlying plasmonic phenomena. The discussion begins with surface plasmon polaritons and progresses to their localized form, localized surface plasmon resonances, first described through the quasistatic approximation and later extended using Mie theory. The chapter concludes with several key remarks concerning the characteristics and relevance of LSPR.

In Chapter 3, we provide an introduction to nanoparticle self-assembly induced by both thermal and laser annealing, with particular emphasis on laser annealing. The theoretical background includes the fundamentals of laser–matter interaction, laser-induced heating and thermoplasmonic effects.

Subsequently, Chapter 4 details all practical aspects of this study, including the sample preparation procedures, the laser annealing setup, the developed spectrometry system and the techniques used for morphological characterization.

The results are presented in Chapter 5, comprising the transmittance spectra, SEM micrographs and nanoparticle size distribution histograms. This chapter also includes a numerical model describing the extinction cross sections and estimating the temperature rise during irradiation.

Finally, in Chapter 6, we summarize the main achievements of this work and provide perspectives for future research directions.

Chapter 2

Nanoparticle plasmonics

The unique optical properties of metals, which are the foundation of plasmonics, arise from the distinct nature of their electronic structure. In contrast to insulators or semiconductors, where electrons are tightly bound to individual atoms or covalent bonds, the valence electrons in a metal are delocalized, forming a highly mobile "sea" of charge that permeates a fixed, positively charged ionic lattice. This arrangement is often conceptualized through simplified yet powerful theoretical frameworks, such as the Drude or the jellium models, in which the discrete lattice of positive ion cores is treated as a uniform background of positive charge, providing a neutralizing medium for the free electron gas [12]. The defining characteristic of this system is the exceptionally high density of free charge carriers, typically on the order of 10^{23} electrons/cm^3 in common metals [13]. It is this high density that enables a collective, rather than individual, electronic response to external stimuli.

When an electromagnetic wave, such as light, interacts with a metal, its oscillating electric field component exerts a periodic Coulomb force on the electron gas. Because the electrons are not bound to specific atomic sites, they are free to move in response to this external field. In the classical picture, the electric field displaces the electron cloud relative to the essentially stationary positive ion cores. This charge separation induces a net negative surface charge on one side of the material and leaves a net positive charge on the other. This induced charge distribution generates a powerful internal electric field that acts as a restoring force, pulling the displaced electron cloud back toward its equilibrium position. However, upon returning to equilibrium, the inertia of the electrons causes them to overshoot, leading to a charge displacement in the opposite direction. This process repeats, establishing a robust, collective oscillation of the entire electron gas density, which is known as a plasma oscillation. This dynamic can be modeled as a simple harmonic oscillator, where the electron cloud is the mass and the Coulomb attraction to the ion lattice provides the restoring spring force. The natural frequency of this oscillation, ω_p, is a fundamental property of the metal itself and is called the plasma frequency.

What this fundamental framework ultimately illustrates is that the interaction of light with a metal is

not a series of isolated events involving single electrons. Instead, the long-range nature of the Coulomb force, combined with the high density of charge carriers, ensures that the motion of any given electron is strongly correlated with the motion of its neighbors [14]. This coupling forces the entire electron gas to respond to an external field in a coherent and organized way. This collective behavior is the defining characteristic that distinguishes plasmonics from the excitonic physics of semiconductors.

2.1 Surface Plasmon Polaritons

Like many other physical entities, such as light or electrons, the plasma oscillations also exhibit wave-particle duality. The quantization of these oscillations was first proposed in 1952 by David Pines and David Bohm and their quantum is the plasmon [15].

Although plasmons can exist as longitudinal waves within the bulk of a metal, the main focus of the field of plasmonics are surface plasmons, excitations that exist only in the surface between a metal and a dielectric. When an incident electromagnetic field penetrates slightly in a planar metal surface, it induces a plasma oscillation, from which another electromagnetic field, that counteracts the initial one, arises. This coupling between the photons and the plasmons forms a new hybrid quasiparticle, the surface plasmon polariton (SPP).

Consider an EM wave with wave vector $\mathbf{k_2} = (k_{2x}, 0, k_{2z})$ propagating in a dielectric medium with $\varepsilon_2 > 0$ and inciding in a metal surface with $\mathbb{R}\mathrm{e}\{\varepsilon_1\} < 0$. From the boundary conditions for the electric fields, the continuity of the tangential electrical field implies that $k_{1x} = k_{2x}$. Using the dispersion equation

$$k_{1x}^2 + k_{1z}^2 = \varepsilon_1 \mu \omega^2 \tag{2.1}$$

we determine that $k_{1z} < 0$. This result implies that there are no waves propagating normal to the surface, there are only evanescent fields, which makes the SPPs highly confined to the interface between the metal and the dielectric, as exemplified in Fig. 1.

A detailed description and derivation of the fields that form SPP. can be found in [17], but because that is outside the scope of this work, we will focus only on the most important equation, the dispersion relation for the SPP.

$$k_{SPP} = \pm \frac{\omega}{c} \sqrt{\frac{\varepsilon_1 \varepsilon_2}{\varepsilon_1 + \varepsilon_2}} \tag{2.2}$$

We know that $\varepsilon_1 \varepsilon_2 < 0$, so for k_x to be real it is necessary that $\varepsilon_1 + \varepsilon_2 < 0$.

A photon propagating in free space with frequency ω has wave vector $k_0 = \frac{\omega}{c}$, so according to

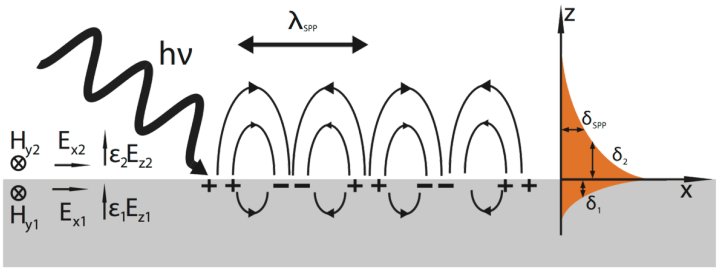


Figure 1: Schematic of an SPP propagating along a metal–dielectric interface, showing the electric and magnetic field components, surface charge oscillations, and evanescent field decay with penetration depths δ_1 and δ_2. Reproduced from [16].

Eq. (2.2), an SPP with the same frequency has wave vector $k_{SPP} > k_0$. This condition implies that surface plasmons cannot be excited by light in normal conditions, they require special mechanisms like the Otto or Kretschmann configurations. This inherent restriction highlights a key motivation behind the study of localized plasmons in nanoparticles, which naturally overcome this limitation through spatial confinement, as we will see in the next section.

2.2 Localized Surface Plasmon Resonance

The physics of surface plasmons undergoes a dramatic transformation when the geometric confinement is increased. When a surface plasmon is confined within a conductive nanoparticle whose dimensions are much smaller than the wavelength of incident light, the excitation is no longer a propagating wave, but a localized surface plasmon (LSP) (Fig. 2). In this regime, the collective oscillation of conduction electrons becomes spatially restricted to the nanoparticle, leading to the formation of strong, non-propagating electromagnetic fields near its surface.

2.2.1 Quasistatic approximation

For nanoparticles much smaller than the wavelength of light, it is possible to neglect the spatial variation of the electromagnetic field across the nanoparticle, allowing the problem to be treated within the quasistatic approximation.

In this framework the system can be analyzed simply by solving the Laplace equation for the electrostatic potential.

$$\nabla^2 V(\mathbf{r}) = -\frac{\rho(\mathbf{r})}{\varepsilon(\mathbf{r},\omega)} \tag{2.3}$$

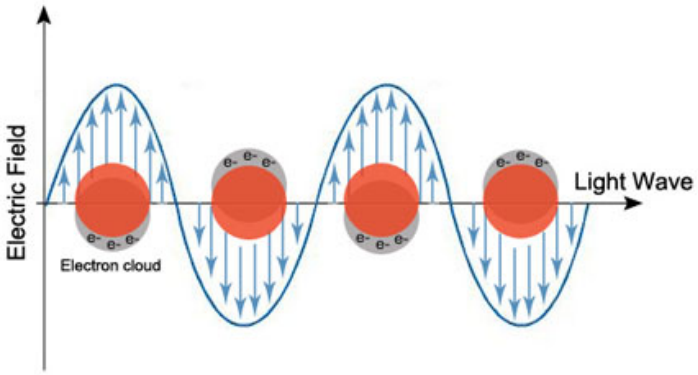


Figure 2: Schematic of a localized surface plasmon resonance (LSPR) in a metallic nanoparticle, showing the displacement of the electron cloud by the oscillating electric field of the incident light. Reproduced from [18].

Despite its simplicity, this approach offers valuable insight into the optical response of nanoparticles. As the detailed mathematical derivation of these expressions goes beyond the present analysis, the most important results are summarized here, following the formulation presented in [19].

Let us consider a metallic sphere with radius R and permittivity ε_1, placed under the influence of a constant external electric field E_0 in a dielectric medium with permittivity ε_2, as depicted in Fig. 3.

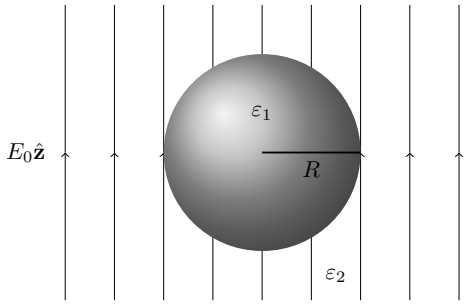


Figure 3: Schematic of a metallic spherical nanoparticle embedded in a dielectric medium under a constant external electric field E_0 applied along the z axis.

By solving Eq. (2.3) it is found that the induced electric potential outside the sphere is of the form of a dipole potential

$$V_2(\mathbf{r}) = \frac{1}{4\pi\varepsilon_2}\frac{\mathbf{p}\cdot\hat{\mathbf{r}}}{r^2} \tag{2.4}$$

Where $\mathbf{p}$ is the dipole moment of the nanoparticle

$$\mathbf{p} = \alpha E_0 \hat{\mathbf{z}} \tag{2.5}$$

and α its polarizability

$$\alpha = 4\pi\varepsilon_2 \left(\frac{\varepsilon_1 - \varepsilon_2}{\varepsilon_1 + 2\varepsilon_2} \right) R^3 \tag{2.6}$$

Even though it is not explicitly written, both permittivities are frequency dependent, and it is important to recall that the dielectric function of metals becomes negative for frequencies below the plasma frequency [12]. Under these conditions, for a particular frequency ω_{LSP}, the real part of the denominator in the polarizability expression approaches zero (it never vanishes completely, as discussed in [19]), leading to a large induced dipole moment and a correspondingly strong localized electric field near the nanoparticle surface.

This phenomenon defines the plasmonic resonance. In contrast to surface plasmon polaritons, which obey a dispersion relation linking the excitation frequency to the in-plane wave vector, the localized surface plasmon is excited at a distinct resonance frequency, independent of the wave vector of the incident light. Consequently, no momentum matching mechanism is required, and LSPs can be directly excited by far field illumination, as well as radiate energy back into the far field.

Using the polarizability we can also write the equations for the scattering and absorption cross sections. The derivation of these equations is available in [20]

$$\sigma_{sca} = \frac{k^4}{6\pi} |\alpha|^2 \tag{2.7}$$

$$\sigma_{abs} = k\, \mathbb{I}\mathrm{m}\{\alpha\} \tag{2.8}$$

We can immediately infer that, like the induced dipole moment, both cross sections exhibit pronounced maxima at ω_{LSP}, often exceeding the geometric cross section of the nanoparticle by several orders of magnitude. This strong enhancement is responsible for the characteristic vibrant colors observed in materials containing metallic nanoparticles, as the famous Lycurgus cup [21]. It is also worth noting that the scattering cross section σ_{sca} scales with R^6 whereas the absorption cross section σ_{abs} scales with R^3, whithin the range of applicability of the quasistatic approximation. Consequently, absorption dominates for smaller particles, whereas scattering becomes increasingly significant as the particle size increases.

2.2.2 Mie theory

Although the quasistatic approximation captures the essential physics of LSPs in small nanoparticles, it becomes inaccurate for larger particles where phase retardation and radiative damping effects cannot be

neglected. In such cases, a complete description was written by Gustav Mie [22], which solves Maxwell's equations exactly for spherical particles of arbitrary size. Mie theory offers a rigorous framework for describing the scattering and absorption of electromagnetic waves by a spherical particle. The incident plane wave is expanded into a series of electric and magnetic multipoles, and the boundary conditions at the particle surface are used to determine the corresponding fields inside and outside the sphere. From these fields, one can compute the extinction, scattering, and absorption cross sections.

Unlike the quasistatic model, which considers only the dipolar response and neglects retardation, Mie theory inherently accounts for phase variations across the particle and includes contributions from higher-order multipoles. Consequently, it accurately describes phenomena such as the redshift and broadening of the plasmon resonance with increasing particle size, as well as the emergence of quadrupolar and higher-order modes. The total extinction cross section $\sigma_{ext} = \sigma_{sca} + \sigma_{abs}$ and scattering cross section σ_{sca} can be expressed as a sum over some multipole orders

$$\sigma_{ext} = \frac{2\pi}{k^2} \sum_{l} (2l+1) \left(|a_l|^2 + |b_l|^2 \right) \tag{2.9}$$

$$\sigma_{sca} = \frac{2\pi}{k^2} \sum_{l} (2l+1) \, \mathbb{R}\mathrm{e}\{a_l + b_l\} \tag{2.10}$$

Where a_l and b_l are the Mie coefficients representing the electric and magnetic multipole contributions, respectively. A detailed derivation of these coefficients is beyond the scope of this work, and the results presented here follow the formulation given in [19].

Mie theory thus provides a comprehensive understanding of how nanoparticle size influences the optical response, bridging the gap between the quasistatic approximation and the full electrodynamic behavior of larger particles. It forms the theoretical foundation for interpreting the experimental extinction spectra of metallic nanoparticles with varying dimensions and dielectric environments.

2.3 Calculation of extinction efficiencies for case examples

The study of nanoparticle plasmonics shows how the interaction between light and free electrons in metals changes with spatial confinement. Starting from delocalized surface plasmon polaritons that propagate along planar metal–dielectric interfaces, further confinement to subwavelength metallic nanoparticles gives rise to localized surface plasmons, non-propagating resonances that produce strong electric field enhancement and are extremely sensitive to the surrounding dielectric environment.

The position and intensity of the localized surface plasmon resonance depend strongly on several

factors. As the particle size increases, the resonance redshifts and broadens, mainly due to retardation and radiative damping effects (Fig. 5). The dielectric constant of the surrounding medium also plays a key role, since higher refractive indices shift the resonance to lower frequencies (Fig. 6). Moreover, when the nanoparticle departs from a perfect spherical shape, for example becoming elongated or flattened, multiple plasmon modes can appear, each associated with oscillations along different axes (Fig. 4). The optical properties discussed here form the foundation of nanoparticle-based plasmonics. These properties not only determine the optical response of isolated nanoparticles but also become crucial when they are incorporated into more complex architectures.

When metallic nanoparticles are embedded in thin films, their strong near-field interactions and high sensitivity to the surrounding medium allow subtle variations in refractive index or film composition to be detected through measurable shifts in the LSPR frequency. Such hybrid systems combine the tunability of thin-film fabrication with the strong field enhancement of plasmonic nanoparticles, paving the way for advanced sensing applications and integrated photonic devices.

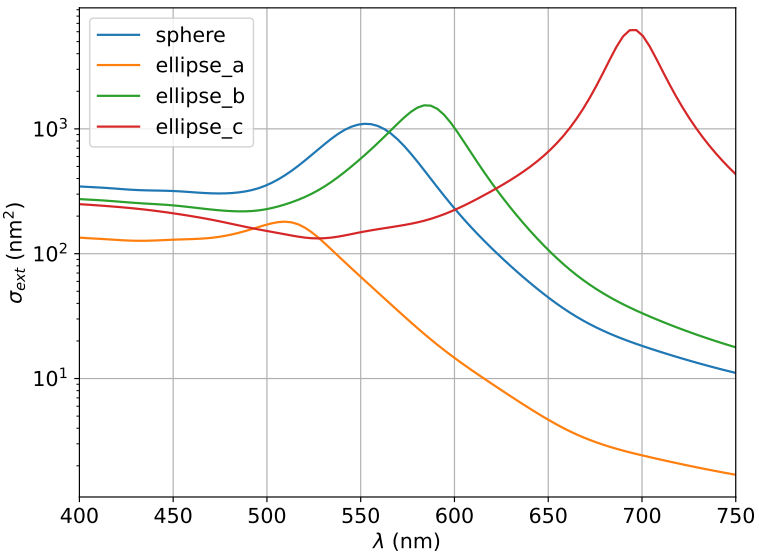
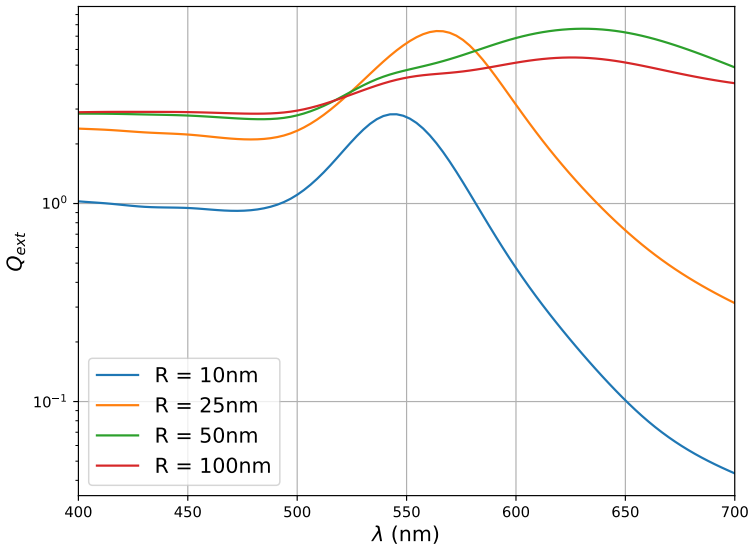
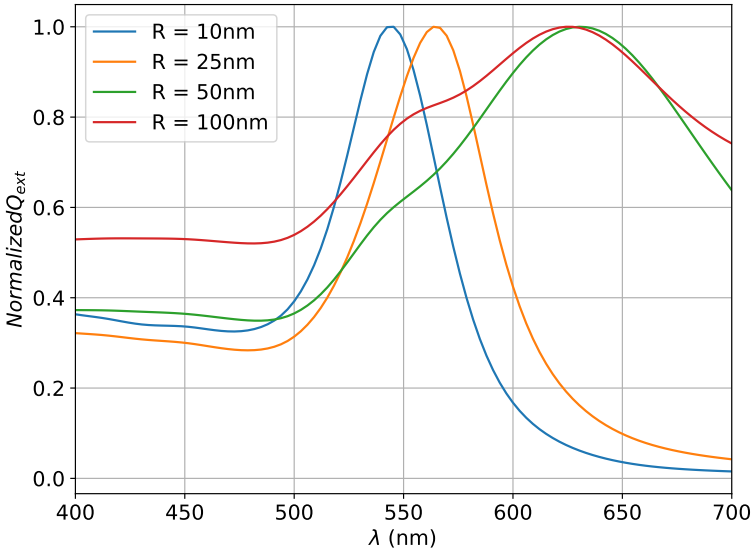


Figure 4: Comparison of the extinction cross sections (σ_{ext}) for a spherical gold nanoparticle ($R = 10\,\text{nm}$) and an ellipsoidal gold nanoparticle ($a = 5\,\text{nm}$, $b = 10\,\text{nm}$, $c = 15\,\text{nm}$) in a dielectric medium with permittivity $\varepsilon = 3$. The spectra are shown for light polarized along each principal axis, highlighting the splitting of the plasmon resonance due to shape anisotropy. Simulated using the MNPBEM software [23].

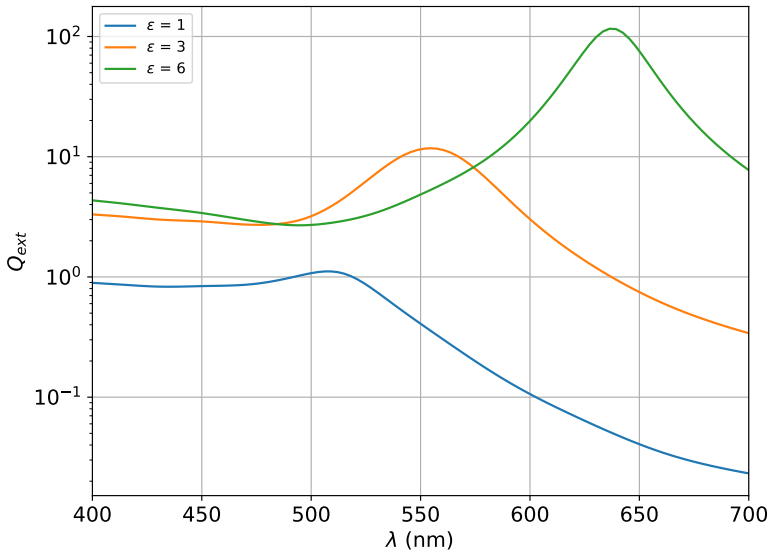


(a)

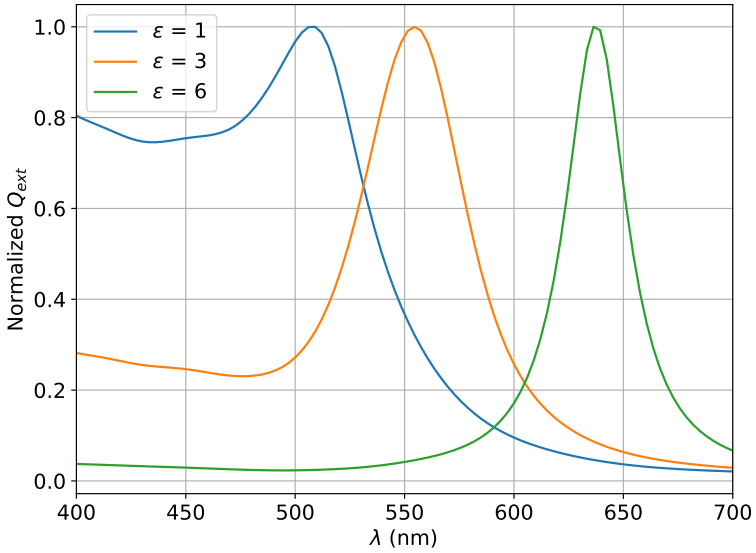


(b)

Figure 5: Extinction efficiency ($Q_{\text{ext}} = \frac{\sigma_{ext}}{\pi R^2}$) of a spherical gold nanoparticle embedded in ZnO [24], shown for different particle radii, highlighting the shifting of the plasmon resonance due to change in size. Simulated using the MNPBEM software [23].



(a)



(b)

Figure 6: Extinction efficiency ($Q_{\text{ext}} = \frac{\sigma_{ext}}{\pi R^2}$) of a spherical gold nanoparticle with radius $R = 25\,\text{nm}$, shown for different medium electric permittivities, highlighting the shifting of the plasmon resonance due to change in medium permittivity. Simulated using the MNPBEM software [23].

Chapter 3

Self-assembly of nanoparticles

According to a classic definition by George M. Whitesides, "Self-assembly is the autonomous organization of components into patterns or structures without human intervention." [25]. In essence, individual building blocks (atoms, molecules, or nanoparticles) spontaneously arrange themselves into larger, more complex patterns driven by their inherent interactions and a tendency to minimize free energy [26]. In practice, self-assembly can be static, when particles arrange themselves without the need of external energy, or dynamic, where an ongoing supply of energy (thermal, magnetic, optical, etc.) continuously influences the assembly process.

Gaining control over a process that is inherently self-driven is one of the biggest obstacles in this field. The ultimate objective of nanotechnology is to consistently create distinct, well-defined structures, even though self-assembly naturally implies a spontaneous and autonomous organization. This apparent contradiction can be overcome by realizing that control in self-assembly does not come from manipulating each particle individually, but rather from carefully tuning the energetic and kinetic conditions that guide their collective behavior. In this way, the emphasis shifts from direct fabrication to programming the material and its surroundings, incorporating the "instructions" for the intended structure into the surface characteristics, interactions, and processing parameters.

In the context of this work, the focus is on dynamic self-assembly processes driven by thermal and optical energy inputs.

3.1 Thermal annealing

One effective way to drive the self-assembly or structural evolution of nanoparticles in thin films is through thermal annealing. When a nanocomposite thin film is heated, several processes can occur that cause the nanoparticles to grow, move, or reorganize into a lower energy configuration. Thermal energy increases atomic mobility, allowing particles to overcome kinetic barriers and reconfigure. Two key phenomena

often observed are particle coalescence (when nanoparticles in close proximity merge into larger particles to reduce total surface energy) and Ostwald ripening (when smaller particles dissolve and their atoms redeposit onto larger ones) [27].

For example, in [28], Borges et al. studied Au–TiO_2 nanocomposite thin films (gold nanoparticles embedded in a titanium dioxide matrix) and showed that post-deposition thermal annealing caused significant nanoparticle growth and reorganization . In their system, films annealed at temperatures up to $700\,^{\circ}$C exhibited diffusion of Au within the TiO_2 and the progressive formation of larger Au nanoparticles throughout the matrix . Small gold clusters acted as nucleation sites and grew larger as the temperature increased. At the highest annealing temperatures, evidence suggested that adjacent nanoparticles coalesced and Ostwald ripening took place, yielding a structure with fewer but larger gold particles . As a direct consequence of this thermally induced self-assembly, the plasmonic optical response of the films was dramatically enhanced. Thus, thermal self-assembly in such nanocomposite films is not only a structural phenomenon but also leads to tunable functional properties.

3.2 Laser annealing

While thermal annealing exposes the entire sample to elevated temperature for extended periods (minutes or hours), laser annealing offers a very different and highly localized approach to induce nanoparticle self-assembly. In laser annealing, a laser beam is used as a heat source to rapidly raise the temperature of the material in specific regions. For films containing nanoparticles, especially those with plasmonic metallic nanoparticles, like gold or silver, laser light can be absorbed strongly by the nanoparticles and converted into heat, a concept at the core of thermoplasmonics. Guillaume Baffou's Thermoplasmonics book [29] provides a theoretical framework for how light interacting with metal nanostructures produces heat, and how this process can be harnessed in various ways.

There are three important time scales associated with nanoparticle heating by a pulsed laser [30]: pulse duration, τ_p, which governs how fast the total pulse energy is transferred to the electron gas of the NP; the time constant of electron–phonon interaction, τ_{ep}, approximately equal to $1.7\,$ps for gold, that dictates how long it takes for the energy to be transferred from the electrons to the lattice, thus effectively heating the NP; and the characteristic time of nanoparticle cooling, that is associated with the nanoparticle size, volumetric heat capacity and the medium's thermal conductivity, and controls the rate at which heat is transferred from the particle to the surrounding medium, usually in the order of pico to nanoseconds.

Changing these time scales gives us different heating scenarios. If we used a femtosecond laser, as

the pulse duration is much smaller than τ_{ep}, the totality of the pulse energy is absorbed by the electron gas before it is dissipated into the lattice, heating the particle all at once, as studied in [31]. In the nanosecond scenario, while the energy is still being transferred from the light to the electron gas, a part of it is already dissipating through phonons from the nanoparticle to the surrounding medium.

A successful example of nanosecond laser annealing is the work from Kalfagiannis et al. [10]. They start by creating silver nanoparticles from a silver thin film by heating it with a nanosecond UV laser, showing the self-assembly on nanoparticles, and consequential appearance of an LSPR band, with the increasing number of applied pulses. They later explore the high absorption efficiency in the visible range, and use a nanosecond 532 nm laser to further tune the particle's diameters.

To interpret and visualize the evolution of these complex processes, we can consider a simple model consisting of an isotropic nanoparticle embedded in an isotropic medium, following the approach in [31]. The temporal and spatial evolution of the temperature can be obtained by solving the heat equation,

$$\rho c \partial_t T(\mathbf{r}, t) - \kappa \nabla^2 T(\mathbf{r}, t) = q(t) \tag{3.1}$$

Considering that only the nanoparticle absorbs the laser radiation, we end up with this system of equations,

$$\begin{cases} \rho_{NP} c_{NP} \partial_t T(\mathbf{r}, t) - \kappa_{NP} \nabla^2 T(\mathbf{r}, t) = q(t) \\ \rho_m c_m \partial_t T(\mathbf{r}, t) - \kappa_m \nabla^2 T(\mathbf{r}, t) = q(t) \end{cases} \tag{3.2}$$

Where $\rho_{NP(m)}$ is the nanoparticle (medium) density, $c_{NP(m)}$ is the specific heat capacity of the nanoparticle (medium), $\kappa_{NP(m)}$ is the thermal conductivity of the nanoparticle (medium) and $q(t)$ is the heat source density given by

$$q(t) = \frac{\sigma_{abs} F}{V_{NP}} p(t) \tag{3.3}$$

Where σ_{abs} is the absorption cross section of the nanoparticle, as we saw in the previous chapter, F is the laser fluence, V_{NP} is the nanoparticle's volume and $p(t)$ the temporal shape of the pulse, which in our case is roughly a gaussian function.

The symmetry of the problem simplifies it further into an 1D problem, and despite its simplicity, this method provides a clear physical intuition while retaining the essential features of the problem.

Chapter 4

Experimental methods

4.1 Sample preparation

A custom-made high-vacuum chamber was used to deposit Au-ZnO thin films, i.e. thin films composed of gold (Au) nanoparticles dispersed in a zinc oxide (ZnO) matrix. A rectangular (200 mm × 100 mm × 6 mm) and high purity (99.99 %) zinc target was used as a cathode for the production of thin films. Twenty gold pellets, each with a total surface area of 16 mm^2 and 0.5 mm thick, were placed symmetrically on the erosion track of the zinc target. Rectangular (25 mm × 9 mm × 1 mm) fused silica (SiO_2) substrates were used for the deposition of thin films. To remove impurities from the surface of the substrates and improve the adhesion of thin films, an argon (Ar) plasma was applied, at a partial pressure of 80 Pa for 10 minutes. This plasma treatment was performed in a Diener (Zepto Type Model) equipment, operating at a power of 50 W, using a 13.56 MHz generator – Capacitive coupled plasma system - and at a base pressure of 20 Pa. The substrates were then placed on the grounded substrate holder of the sputtering chamber, which was pumped down to 5×10^{-4} Pa using a turbomolecular pump (Adixen ATP 400). The thin films' deposition occurred at a working pressure of 4.5×10^{-1} Pa, using Ar as the working gas and oxygen (O_2) as the reactive gas. The Ar and O_2 flows were kept constant during the deposition using gas flows of 25 and 17 sccm. A direct current density of 50 A/m^2 and a (negative) target potential of 400 V were applied to initiate the sputtering process. The target potential (negative voltage) during the deposition was 370 V.

The deposition time was 40 seconds and the deposition rate of the Au-ZnO thin films is 45 nm/min, estimated by scanning electron microscopy imaging, in cross-section. The atomic concentration of Au in the as-deposited film was 19 at.%, determined by Rutherford Backscattering Spectrometry. The size of the nanoparticles for the as-deposited thin film is expected to be lower than 10 nm as usual for this kind of thin film systems [4].

4.2 Laser annealing setup

The laser annealing setup used in this work is illustrated in Fig. 7. To the right we have the laser, followed by the set of optics to adjust the beam power and radius, to the left we have the linear stages and sample holder, all of which are described in the following paragraphs. From bottom to top it is also possible to see the spectrometry monitoring system that is covered in the next section.

To perform the laser annealing on the samples we used the second harmonic ($\lambda = 532$ nm) pulses from a Q-switched Nd:YAG laser by Litron Lasers (model LPY604T-10) with a 10 Hz repetition rate. This laser was chosen because it emits in a wavelength close to the LSP resonance of gold, as we saw in Fig. 6. The average power was measured using a Scientech power meter (model AC2501H). Unfortunately, it is calibrated only for $\lambda = 1064$ nm and its last calibration was done 30 years ago, in 1995, so the values used in this work were just for comparison and to have a reference when switching samples. From the laser specifications, we assume that the pulse energy is in the range of 20 mJ to 40 mJ. Due to an inter-cavity spatial filter the transverse spatial profile of the laser beam is a TEM_{00} mode, a gaussian beam with radius ($1/e^2$) $w = 1.15$ mm and its duration is $\tau_p = 10$ ns.

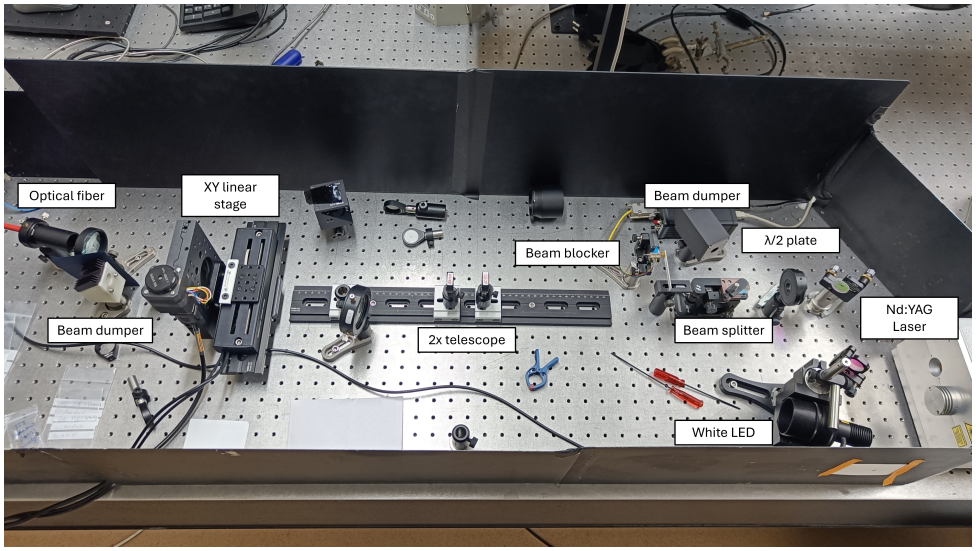


Figure 7: Experimental setup for the laser annealing process, showing the laser source, fluence tuning optics, sample stage, and monitoring system.

The estimated laser fluence, F, is in the range of $1\,\text{J/cm}^2$ to $2\,\text{J/cm}^2$. The reference we had before starting this work was Kalfagianni's paper on laser-induced self assembly of nanoparticles [10], and even though they experimented with silver nanoparticles instead of gold ones as in this work, we tried to use fluence values close to the ones they used (F=$125\,\text{mJ/cm}^2$). To be able to reduce our fluence to more

appropriate values we implemented a Galilean telescope consisting of a concave lens with $f = -50\,\text{mm}$ and a convex lens with $f = 100\,\text{mm}$. This configuration widens the beam to double the initial size, resulting in a fourfold decrease in the fluence values. To have further control of the pulse energy, a half-wave plate was used to change the polarization, followed by a beam splitter to discard the vertical polarization.

Since the laser beam only covers a small fraction of the sample's surface and each spot was irradiated for at least 30 seconds, it would not be feasible to be moving the sample by hand. Two motorized linear stages were combined to perform movements in a plane perpendicular to the laser beam and a custom support was designed in solidworks and 3d printed. We also used a 3d printed blade, connected to a stepper motor to block the laser, since it couldn't be controlled by a computer. Everything was automated and controlled with Python software specifically developed for this project.

4.3 In-situ real-time optical monitoring

In conventional thermal annealing processes, the evolution of the properties of the sample during treatment cannot be directly observed, since the characterization is typically performed only after the annealing step. This limitation makes it difficult to understand what is happening in the material and identify optimal process parameters.

In contrast, the laser annealing setup developed in this work includes an in-situ monitoring system, which enables real time observation of the thin films' response to laser annealing. This capability is particularly valuable in exploratory studies such as the present one, where there is limited prior knowledge regarding the behavior of the material under laser exposure. By monitoring the process as it happens, it becomes possible to correlate experimental parameters such as laser fluence or the number of pulses with immediate material responses, providing insight that would otherwise be lost in a purely post-process analysis.

The simplest and probably most useful monitoring system for this setup is a spectrometry system to observe changes in the transmission spectrum of the thin films. The illumination source initially employed in the setup was a Thorlabs MNWHL4 LED, whose emission spectrum is shown in Fig. 8. Its emission spectrum displayed a pronounced dip near $500\,\text{nm}$, which could affect the detection of the gold localized surface plasmon resonance expected to occur between $500\,\text{nm}$ and $550\,\text{nm}$. Following a device failure, the source was replaced with a "Sun-Like" LED acquired from AliExpress, whose spectral output (Fig. 9) is comparatively flatter across the visible range.

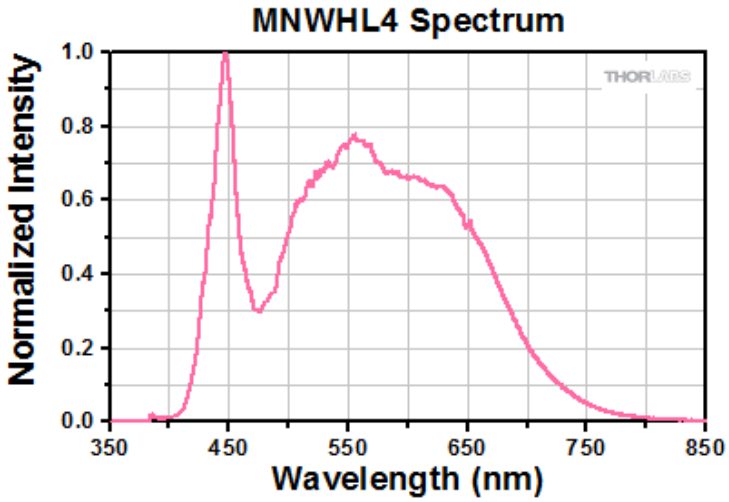


Figure 8: Emission spectrum of the Thorlabs MNWHL4 white light LED. Reproduced from [32]

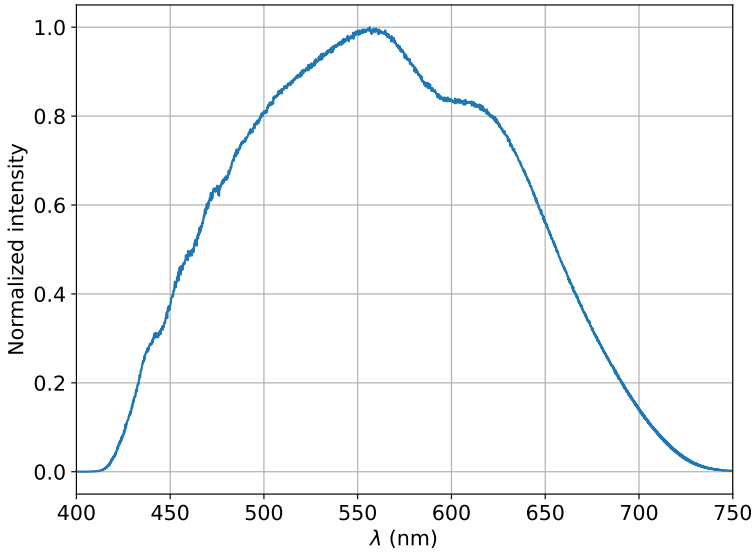


Figure 9: Emission spectrum of the "sun-like" LED.

The optical path of the white light was adjusted so that it overlapped the laser beam on the sample surface, ensuring that both illuminated the same region. It was then collected from the back and focused with a lens on an optical fiber connected to an USB4000 spectrometer from Ocean Optics. A Python script was developed using the Ocean Optics' software development kit, to monitor the transmittance spectrum during the annealing process.

4.4 SEM characterization

The morphology of the Au–ZnO thin films was analyzed by scanning electron microscopy (SEM) using a gaseous analytical detector (GAD) in SEMAT/UM. Prior to imaging, the samples were coated with a thin conductive layer to minimize surface charging effects and improve image quality. Although this procedure reduces charging artifacts, the use of the GAD detector remained advantageous due to its capability to operate under low-vacuum conditions, which further stabilizes the electron signal and enhances image contrast.

The GAD collects a mixed signal composed of secondary and backscattered electrons generated during the electron–sample interaction. The gaseous environment inside the chamber enables ionization cascades that amplify the detected signal and help neutralize residual surface charges [33, 34]. As a result, this detection mode combines topographical information with atomic number (Z) contrast, where regions containing heavier elements appear brighter. In the present case, the gold nanoparticles (Z = 79) stand out clearly against the ZnO matrix (Zn: Z = 30, O: Z = 8), allowing their morphology and distribution to be easily identified.

The SEM images were subsequently analyzed using ImageJ in order to determine the size distribution of the nanoparticles.

Chapter 5

Results and discussion

5.1 Thermal annealing data

The starting point for this study was the previous work on nanoparticle self-assembly by thermal annealing [3, 7]. We compare our findings with those prior results to contextualize and validate the present work.

5.1.1 Spectrometry

The transmittance spectra of the thermally annealed Au-ZnO thin films were measured using a Shimadzu spectrometer. The use of different devices for measuring the spectra explains the different noise levels between the spectra of thermally or laser annealed samples.

Although thermal annealing was performed across a wide temperature range, only the results from selected temperatures are displayed here (Fig. 10). These were chosen based on the magnitude of observed changes, to facilitate comparison without overcrowding the figure.

We can see that the most pronounced dips appear for the films treated at $750\,^{\circ}$C and $800\,^{\circ}$C. The observable drastic blueshift of the LSPR wavelength between both spectra suggests that the gold NPs are increasingly exposed to air. This behavior can be attributed to a decrease in the effective dielectric constant surrounding the NPs, which leads to an increase in the LSPR frequency (see Section 2.3). Among the studied samples, the film treated at $800\,^{\circ}$C exhibits the closest resemblance to the results obtained from laser annealing, as will be discussed in the following sections. Therefore, this condition was selected for direct comparison. The transmittance spectrum of this sample is presented with more detail in Fig. 11, highlighting the central wavelength of the resonance and its full width at half minimum.

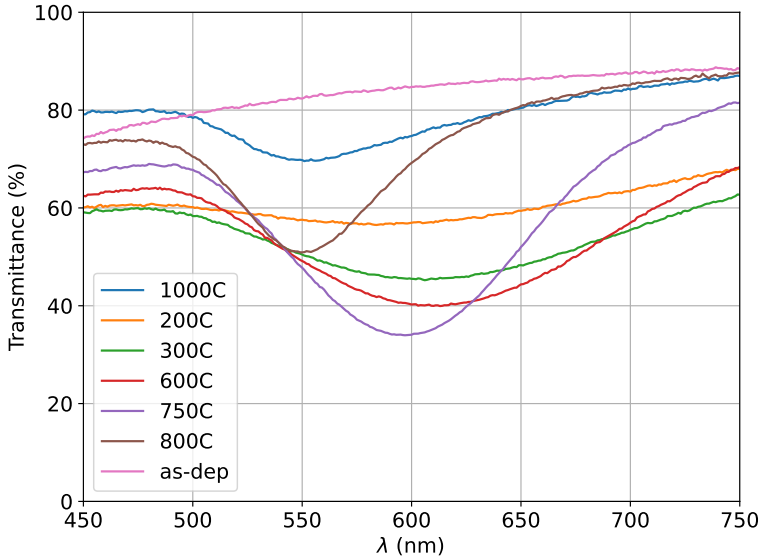


Figure 10: Transmittance spectra of the thermally annealed Au-ZnO thin films comparing the treatments at different temperatures with the as-deposited film.

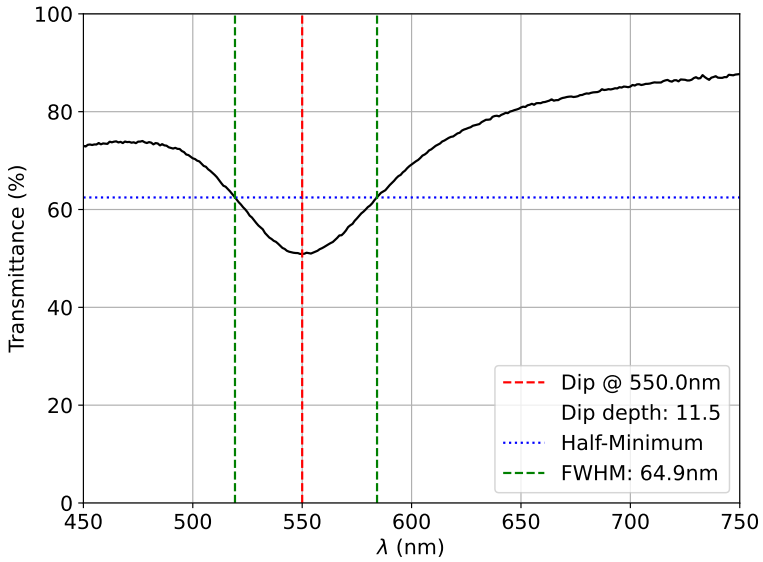


Figure 11: Transmittance spectrum of the Au-ZnO thin film treated at $800\,^{\circ}$C showing the central wavelength of the LSP resonance and the boundaries of the FWHM.

5.1.2 Nano-morphology

The morphology of the thermally annealed Au–ZnO thin films was examined by SEM, as shown in Fig. 12. The corresponding particle size distribution is represented in Fig. 13. The average radius of the nanopar-

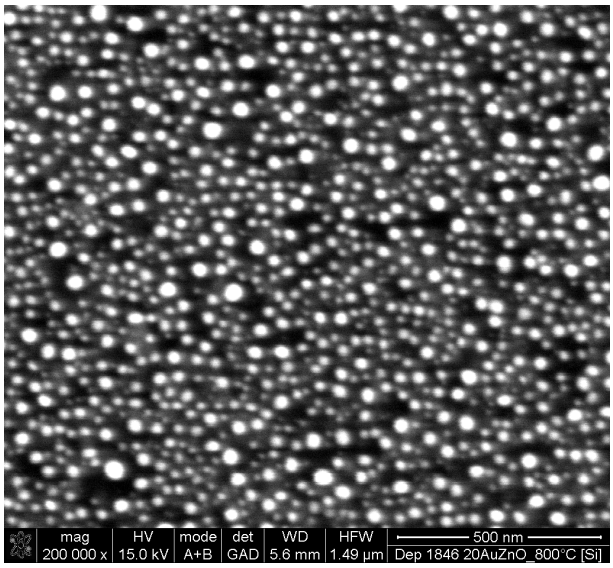


Figure 12: SEM micrograph of thermally annealed Au–ZnO thin film at $800\,^{\circ}\mathrm{C}$.

ticles was about $11.66\,\mathrm{nm}$ ($\sigma = 5.11\,\mathrm{nm}$). Although there is no data regarding the size distribution of the as-deposited samples, it is know from previous similar works that the mean radius is about $3\,\mathrm{nm}$ [4]. These results indicate that the thermal annealing process promotes significant nanoparticle growth, increasing the mean radius by roughly a factor of four and leading to a broader size distribution.

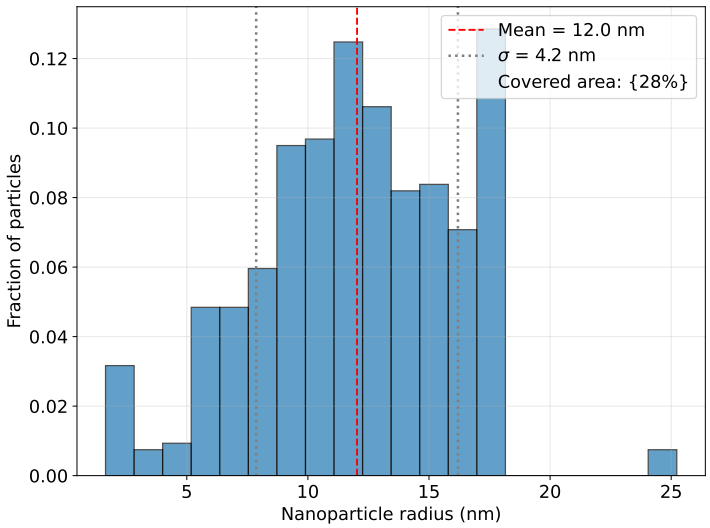


Figure 13: Size distribution histogram of Au NPs corresponding to the SEM image in Fig. 12.

5.2 In-situ spectrometry

The laser annealing process was monitored in situ through real-time transmittance measurements, as previously explained. This enabled the temporal tracking of the LSPR dip. From these data, the evolution

of the dip wavelength, depth and FWHM was extracted, providing direct evidence of nanoparticle growth and plasmonic modification during irradiation.

In Figs. 14 to 16 the temporal evolution of the transmittance spectra is presented for the samples treated at 160 mW, 190 mW and 220 mW, corresponding to four different irradiation times.

The evolution process is qualitatively similar for all three samples. Initially, the overall transmittance decreases until the LSPR dip becomes distinguishable. The number of pulses required for the dip to emerge, however, was observed to vary considerably across different regions of the thin films (approximately ten pulses for the samples shown in Fig. 14 and Fig. 16, and around seventy pulses for the sample in Fig. 15). This behavior suggests that the gold distribution within the as-deposited films is spatially inhomogeneous. After the dip appears, its depth continues to increase slightly, while the transmittance at the side wavelengths increases again, resulting in a more pronounced resonance feature. This effect likely reflects a partial reorganization or coalescence of the nanoparticles, leading to a clearer plasmonic response. This behavior seems to stabilize after hundreds of pulses for all the samples, as no significant changes in the dip wavelength, depth and FWHM seem to occur.

The dip's central wavelength remains practically the same, oscillating around 550 nm, for the duration of the whole process and showing little dependence on laser power. This value is similar to the one measured for the thermally annealed sample, and again suggests that a large volume of the NPs are in contact with the air. The only observed exception is presented first graph of Fig. 16 where the dip is redshifted, possibly meaning that the nanoparticles were still migrating to the surface of the film during the first pulses.

The spectra presented in Fig. 17 were taken in different regions from the ones presented before and the parameters of the LSPR dip are available in Table 1. The difference between these results and the ones analyzed before further supports the idea that the film is inhomogeneous, as these parameter are highly dependent on the gold NPs density and morphology. Overall, no significant differences were detected between the samples annealed at different laser powers. However, a clear distinction arises when comparing laser annealed and thermally annealed samples: the second exhibits a deeper and broader LSPR dip. This difference is likely related to the nanoparticle size distribution, which will be discussed in the following section.

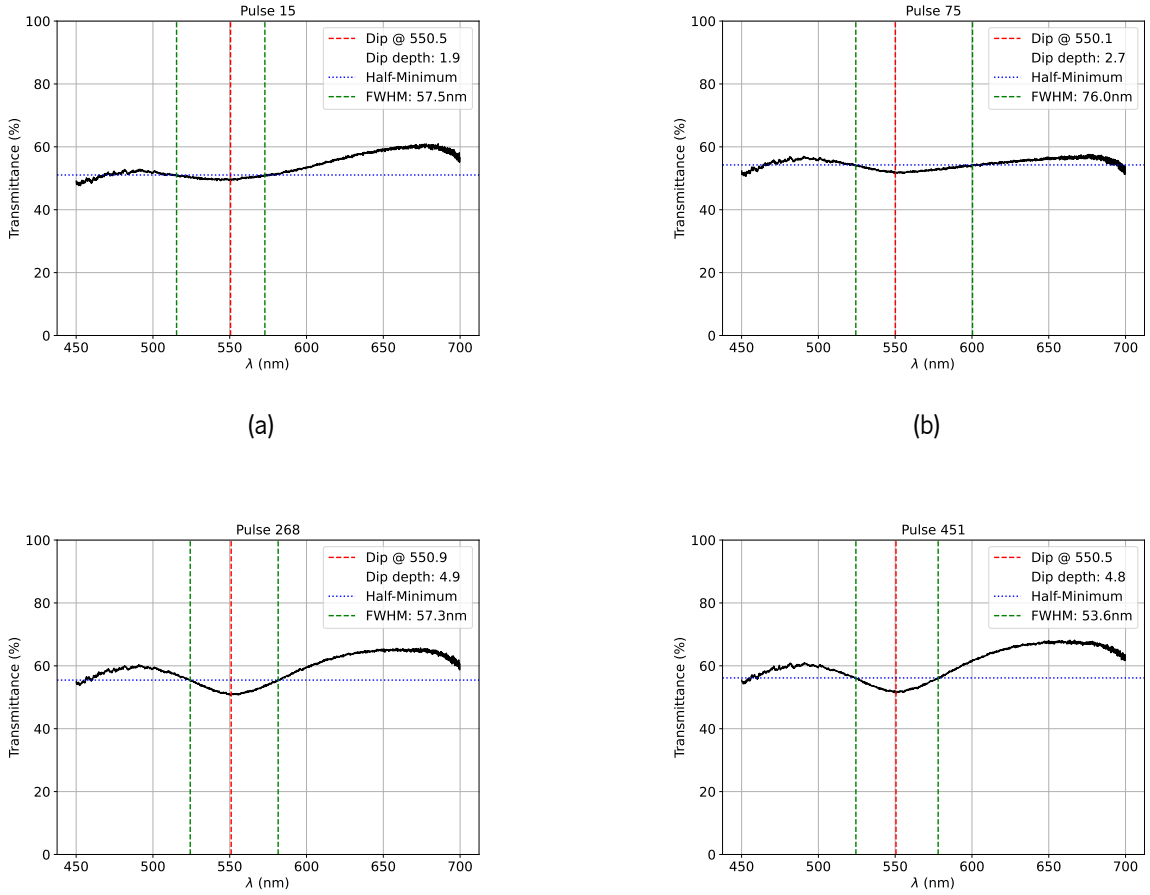


Figure 14: Transmittance spectra of the Au–ZnO thin films treated at 160 mW recorded at successive irradiation times, illustrating the evolution of the LSPR dip position, depth, and FWHM for different number of applied pulses. a) 15 pulses; b) 75 pulses, c) 268 pulses and d) 451 pulses.

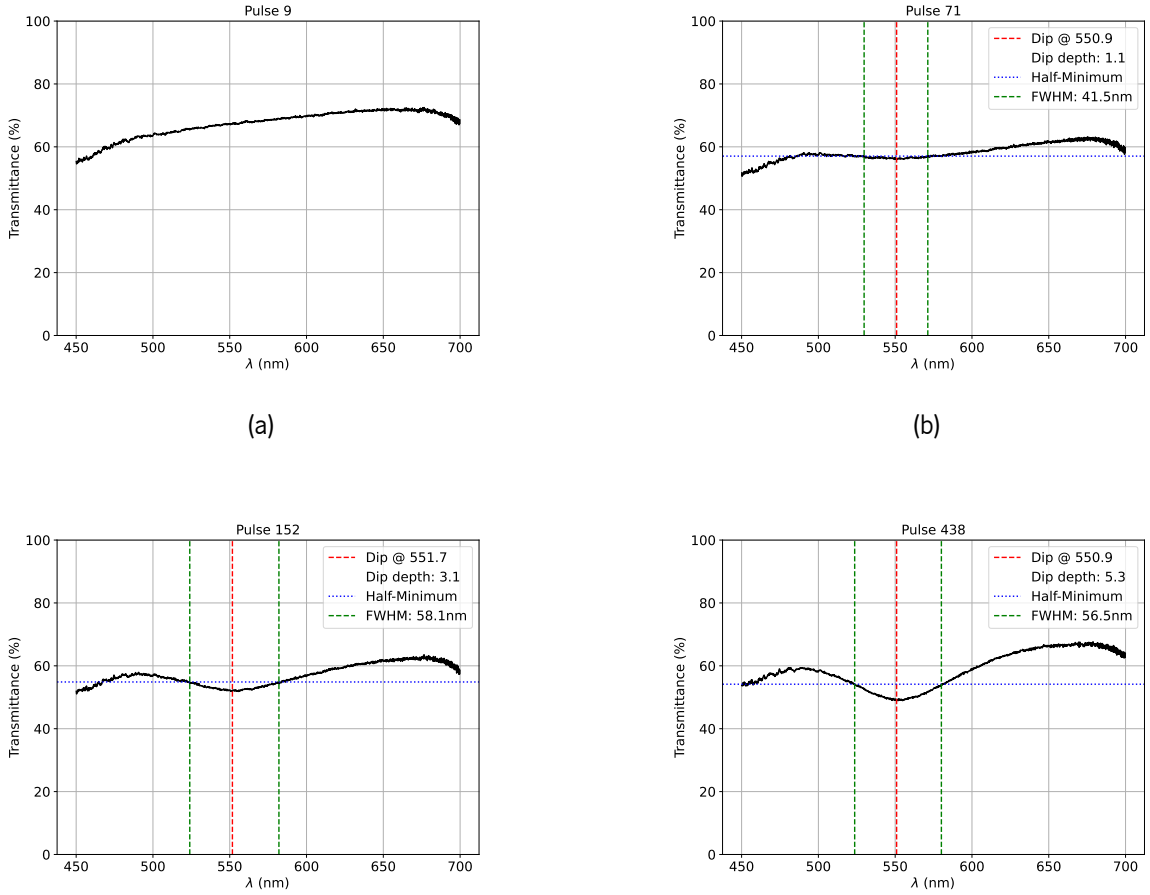


Figure 15: Transmittance spectra of the Au–ZnO thin films treated at 190 mW recorded at successive irradiation times, illustrating the evolution of the LSPR dip position, depth, and FWHM for different number of applied pulses. a) 9 pulses; b) 71 pulses, c) 152 pulses and d) 438 pulses.

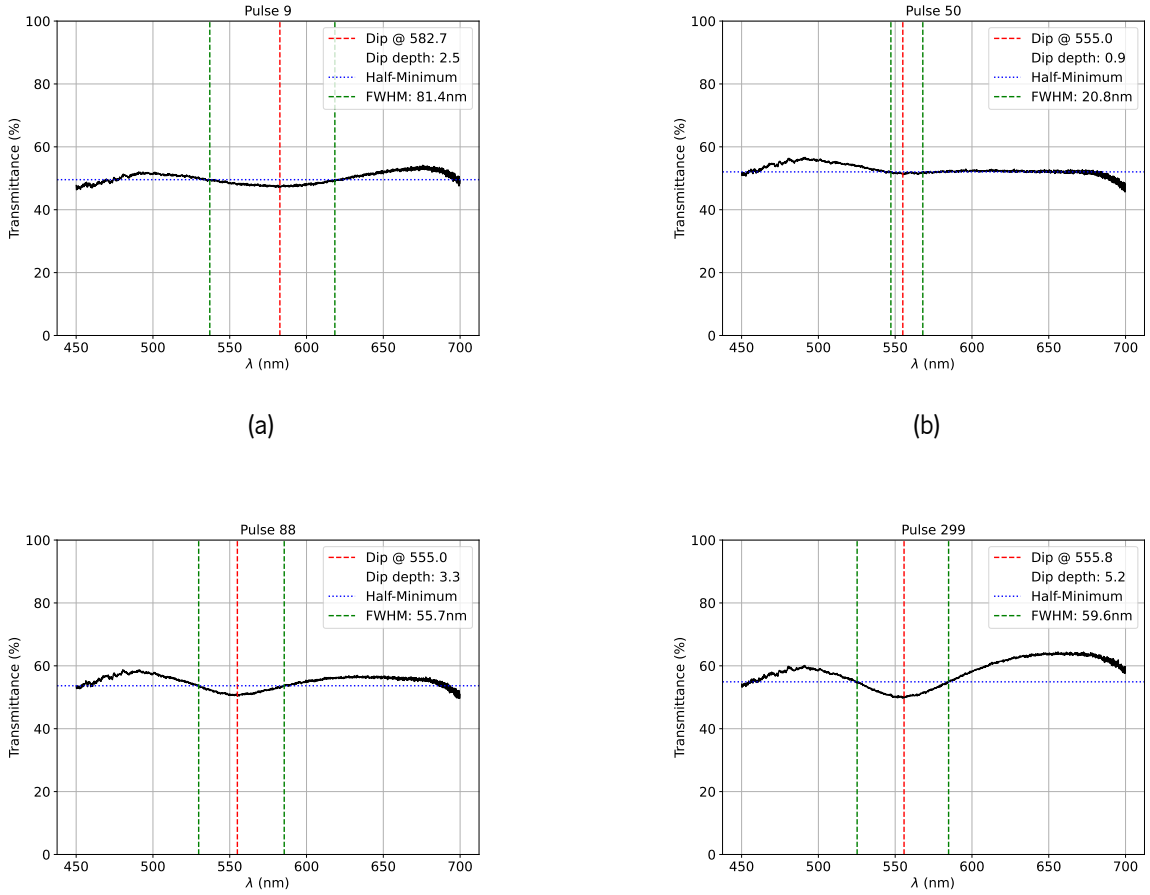


Figure 16: Transmittance spectra of the Au–ZnO thin films treated at $220\,\mathrm{mW}$ recorded at successive irradiation times, illustrating the evolution of the LSPR dip position, depth, and FWHM for different number of applied pulses. a) 9 pulses; b) 50 pulses, c) 88 pulses and d) 299 pulses.

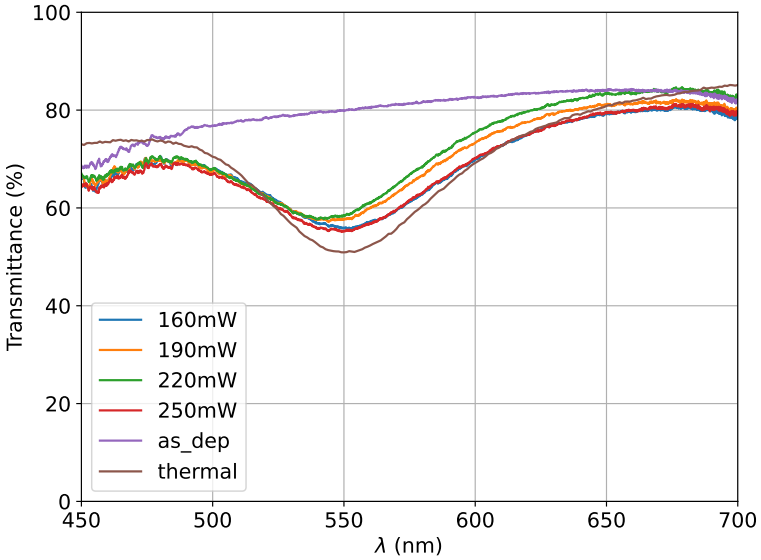


Figure 17: Transmittance spectra of the Au–ZnO thin films after laser annealing with approximately 500 pulses at different laser powers compared to the spectra of the as-depostied and the thermally annealed at $800\,^{\circ}$C samples.

P (mW)	160 mW	190 mW	220 mW	250 mW	Thermal
λ_{Dip} (nm)	553.0	544.1	539.6	549.3	550.0
Dip depth	7.6	6.5	6.6	7.1	11.5
FWHM (nm)	61.6	55.4	53.8	58.6	64.9

Table 1: Optical parameters of the LSPR dip for different laser powers and for the thermally annealed sample. Associated with Fig. 17.

5.3 Morphological analysis

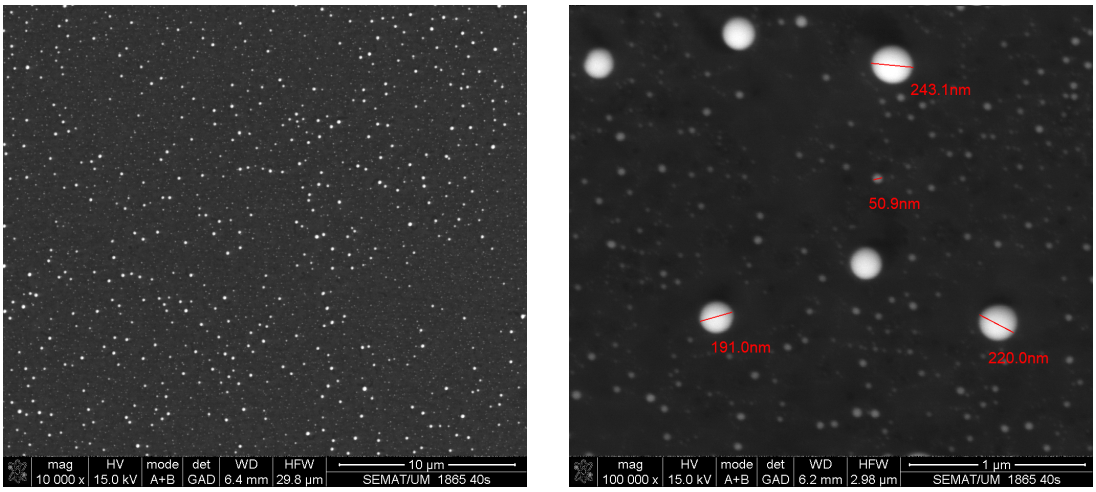
To complement the optical analysis and clarify the structural origins of the observed plasmonic behavior, the morphology of the laser annealed Au–ZnO thin films was examined by scanning electron microscopy. The analyzed thin films were the same ones whose spectra was presented in Fig. 17, processed with 500 pulses at 4 different powers (160 mW, 190 mW, 220 mW and 250 mW). The micrographs in Figs. 18a, 19a, 20a and 21a provide direct evidence of nanoparticle formation and growth, enabling the evaluation of particle size, distribution, and surface coverage. From these images, the nanoparticle size distributions were extracted using ImageJ, allowing a quantitative comparison between the different annealing methods.

This analysis offers further insight into the relationship between the morphology of the films and their corresponding optical responses. The results are available in Figs. 18b, 19b, 20b and 21b and Tables 2 to 5

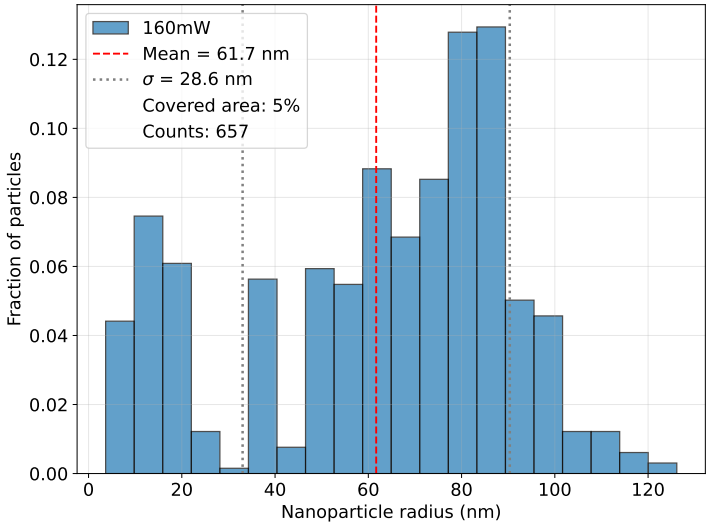
In comparison with the thermal annealing results, the laser annealed films exhibit less controlled nanoparticle growth, result in a much larger average radius and also in a broader distribution of sizes. Similar to the spectra, the average radius doesn't seem to have any correlation with incident beam energy, instead it probably depends on the observed region. In the right image of Fig. 21a the density of smaller NPs is lower than in Figs. 18a, 19a and 20a, which results in less counts for small NPs, and thus in an increase in the average nanoparticle radius. Another example is the increase in the average radius when going from the sample treated at 160 mW to the one treated at 190 mW but then dropping again in the sample treated at 220 mW.

Another marked difference is the surface area covered by nanoparticle, which went from 28% in the thermally annealed sample to approximately 5% across all laser annealed samples. This result is expected because as the average radius increases, the particle number density drops, leading to a smaller overall covered area. Such behavior is typical of Ostwald ripening or particle coalescence, where larger nanoparticles grow at the expense of smaller ones. Additionally, local inhomogeneities in the initial gold distribution and in the laser-induced temperature field can enhance these effects, producing the regional variations observed among the samples. Finally it is possible that some of the gold was lost due to evaporation from the surface.

In all the histograms we can also observe that there seems to be a lack, or reduced number of particles with radii between 20 nm to 40 nm. A possible explanation for this behavior is that neighboring nanoparticles merge into larger ones, which eventually become sufficiently isolated and stop growing further. This process could lead to a quasi–steady state, as observed in the spectrometric data, where no significant evolution of the LSPR band occurs with additional laser pulses.



(a)

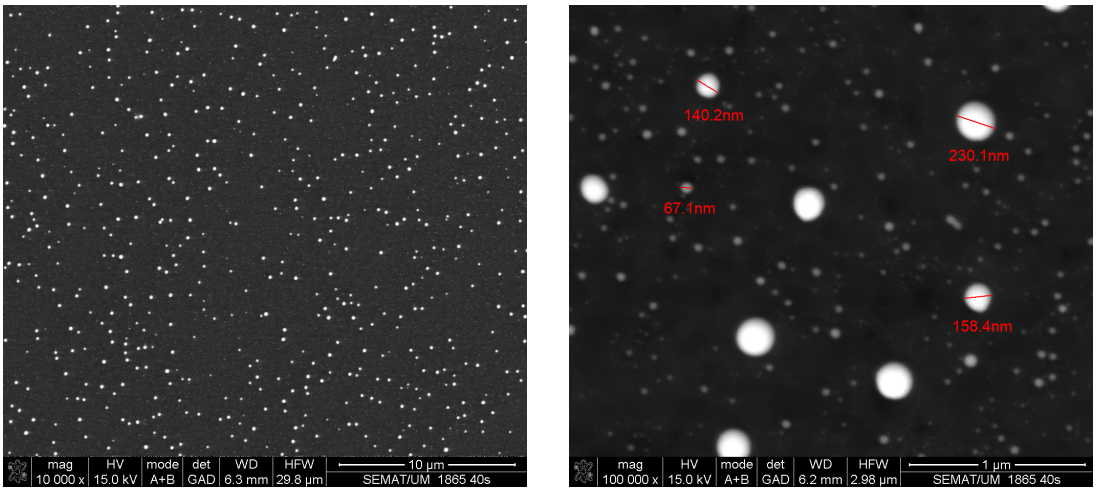


(b)

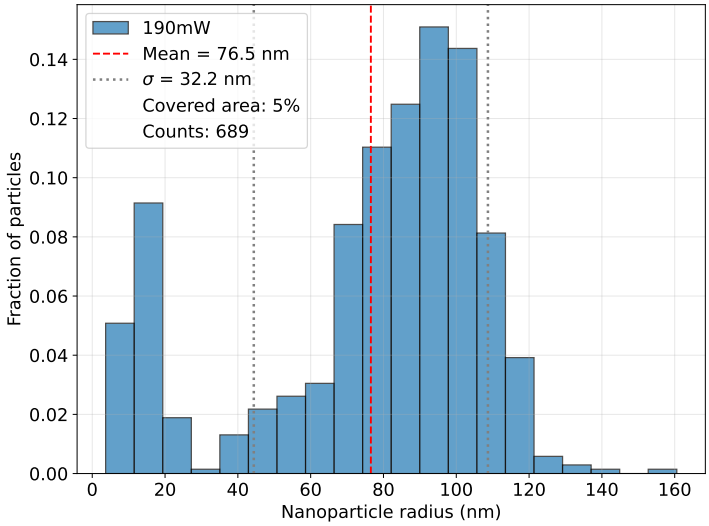
Figure 18: Morphological characterization of the Au–ZnO thin film treated at 160 mW. a) SEM micrographs for different laser powers and b) corresponding nanoparticle size distribution.

Nanoparticle counts	Average radius (nm)	σ (nm)	Surface coverage (%)
657	61.7	28.6	5

Table 2: Nanoparticle counts, average nanoparticle radius, standard deviation, and estimated surface coverage obtained from SEM image analysis of the sample treated at 160 mW.



(a)

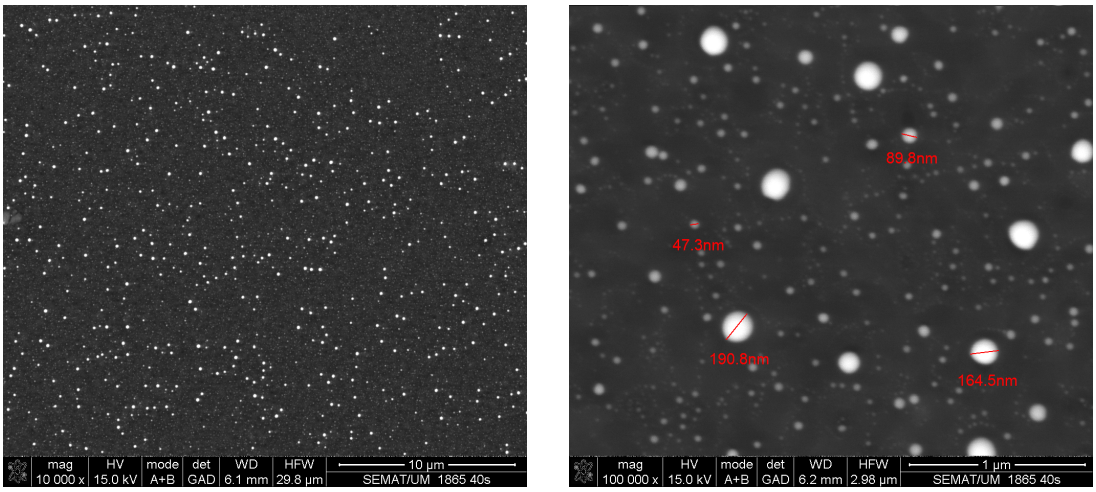


(b)

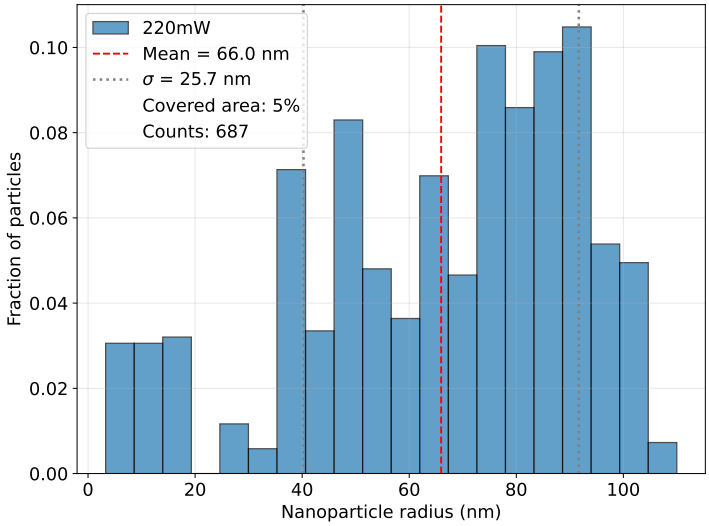
Figure 19: Morphological characterization of the Au–ZnO thin film treated at 190 mW. a) SEM micrographs for different laser powers and b) corresponding nanoparticle size distribution.

Nanoparticle counts	Average radius (nm)	σ (nm)	Surface coverage (%)
689	76.5	32.2	5

Table 3: Nanoparticle counts, average nanoparticle radius, standard deviation, and estimated surface coverage obtained from SEM image analysis of the sample treated at 190 mW.



(a)

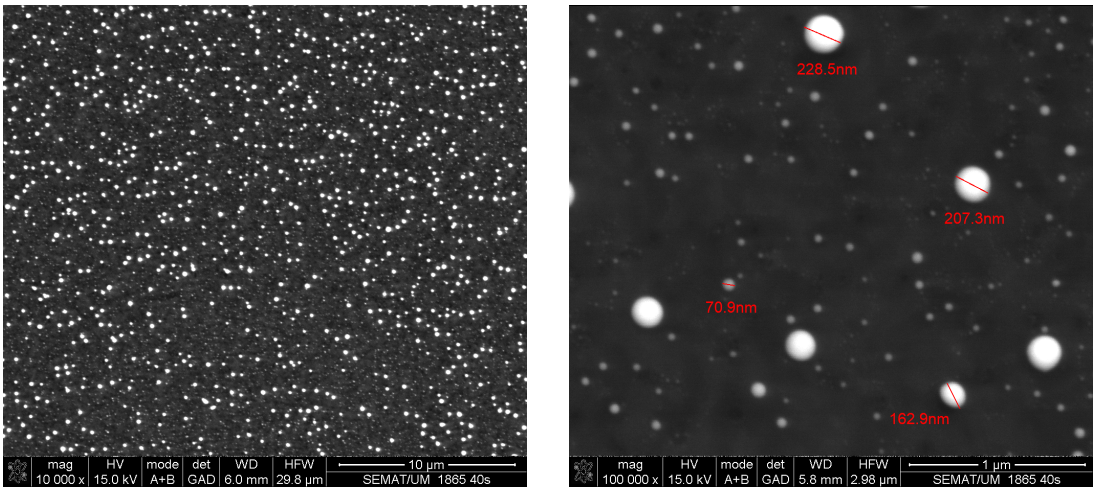


(b)

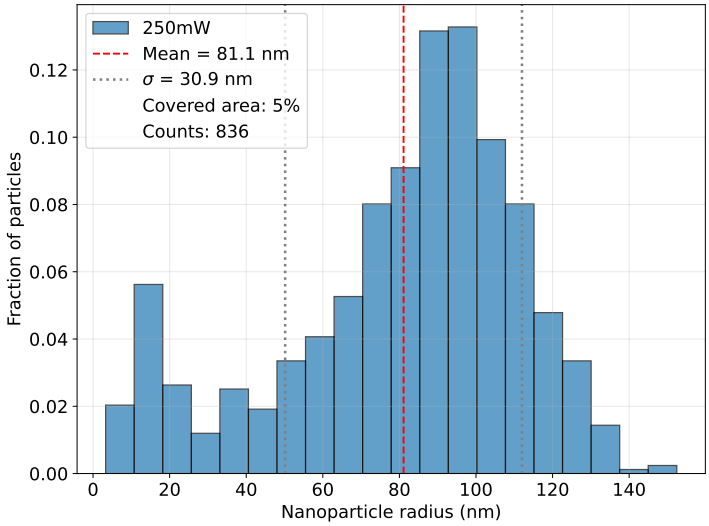
Figure 20: Morphological characterization of the Au–ZnO thin film treated at 220 mW. a) SEM micrographs for different laser powers and b) corresponding nanoparticle size distribution.

Nanoparticle counts	Average radius (nm)	σ (nm)	Surface coverage (%)
687	66.0	25.7	5

Table 4: Nanoparticle counts, average nanoparticle radius, standard deviation, and estimated surface coverage obtained from SEM image analysis of the sample treated at 220 mW.



(a)



(b)

Figure 21: Morphological characterization of the Au–ZnO thin film treated at 250 mW. a) SEM micrographs for different laser powers and b) corresponding nanoparticle size distribution.

Nanoparticle counts	Average radius (nm)	σ (nm)	Surface coverage (%)
836	81.1	30.9	5

Table 5: Nanoparticle counts, average nanoparticle radius, standard deviation, and estimated surface coverage obtained from SEM image analysis of the sample treated at 250 mW.

5.4 Numerical modeling

To complement the experimental results, it is useful to develop numerical models that help reproduce and better understand the observed behavior. One of the problems we can think of when analyzing the size histograms is that we have nanoparticles much bigger than the thin film thickness, which is about 30 nm, obtained from the values described in Section 4.1. This raises several questions: Are some of these particles partially embedded within the film while others are exposed on the surface? Are they truly spherical, or do they merely appear so in the two dimensional SEM images?

In Fig. 22 we compare the extinction efficiency of a 70 nm radius sphere fully surrounded by air or fully embedded in a ZnO thin film. We can conclude that to have a resonance centered at about 550 nm, a fraction of the sphere should be inside the thin film and the rest in contact with the air. Because this configuration is difficult to model directly, we adopted an approximate approach by considering a spherical gold nanoparticle in air, coated with a ZnO shell. By varying the shell thickness, we can simulate different effective fractions of the nanoparticle volume embedded in the film. In Fig. 23 we plot the extinction efficiency of a 70 nm radius gold nanosphere with varying ZnO shell volume. The fraction, f, corresponds to the fraction of the nanoparticle's volume that is inside the film. We can see that to have a resonance centered at 550 nm, about 10% to 20% of the sphere should be inside the film. In this scenario most of the particle is in contact with the air.

To understand the thermal effects associated with laser irradiation, we adapted the simulation software developed by [30] to model a 70 nm-radius gold nanoparticle both fully embedded in ZnO and completely exposed to air. The temperature evolution is shown in Fig. 24. Considering that the melting point of gold is around 1300 K and its boiling point around 3200 K, the simulations suggest that nanoparticles embedded in the film can reach melting temperatures, as expected, but the nanoparticles completely surrounded by air, or in good approximation with 80% to 90% of its volume exposed to the air, could exceed the vaporization threshold, potentially leading to partial material loss.

Nevertheless, these results should be interpreted with caution, as the models represent simplified approximations that neglect several physical parameters and interactions. Despite their limitations, they provide a solid conceptual basis for understanding the complex processes involved in laser induced nanoparticle heating and morphological evolution.

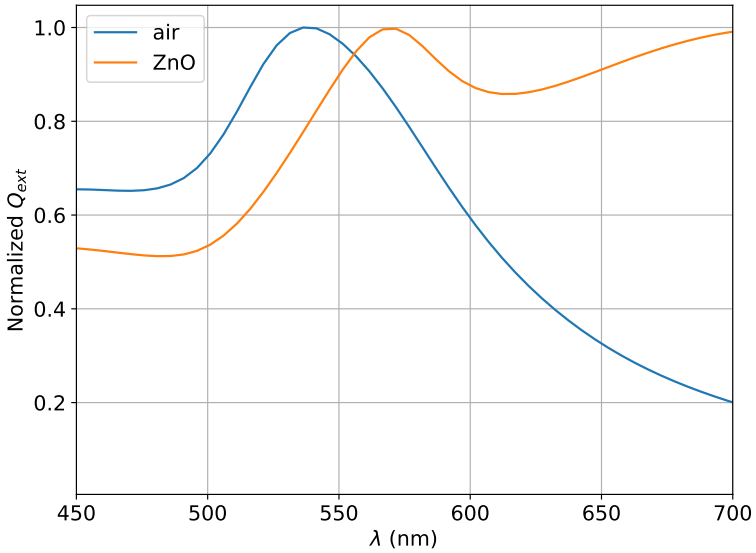


Figure 22: Normalized extinction efficiency ($Q_{\text{ext}} = \frac{\sigma_{ext}}{\pi R^2}$) of a spherical gold nanoparticle with radius $R = 70$ nm, compared in the air and in ZnO thin film. Simulated using the MNPBEM software [23].

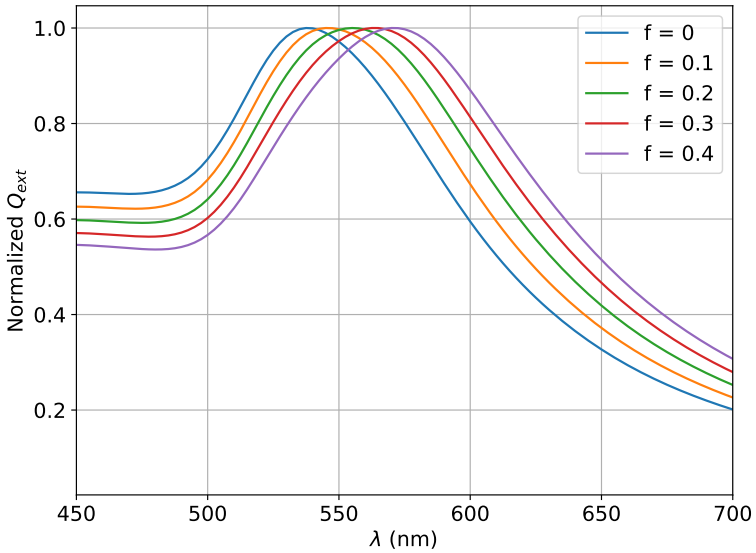


Figure 23: Normalized extinction efficiency ($Q_{\text{ext}} = \frac{\sigma_{ext}}{\pi R^2}$) of a spherical gold nanoparticle with radius $R = 70$ nm, for different values of fraction of shell volume. Simulated using the STRATIFY software [35].

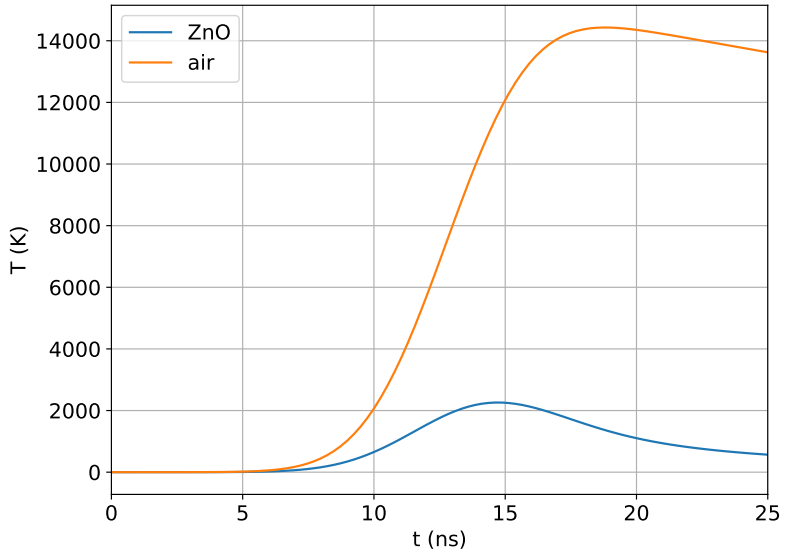


Figure 24: Temporal evolution of the temperature of a spherical gold nanoparticle with radius $R = 70$ nm, under a 10 ns laser pulse with $F = 200\,\mathrm{mJ/cm^2}$ embbeded in a ZnO film or in air.

Chapter 6

Conclusions

In this work, we aimed to evaluate the feasibility of laser annealing as a substitute for conventional thermal annealing. For this purpose, a laser annealing setup was developed based on a nanosecond Nd:YAG laser. Since there was little prior information available on this topic, particularly regarding the laser annealing of thin films containing nanoparticles, the appropriate processing parameters, such as laser fluence and number of pulses, were initially unknown.

To investigate the influence of these parameters, an in-situ spectrometry system was designed and integrated into the setup, using a white LED as the light source and a fiber-coupled spectrometer for real-time transmittance measurements. This configuration successfully allowed the observation of the emergence and evolution of the localized surface plasmon resonance, enabling the correlation of the spectral changes with the applied laser power and number of pulses.

The processed films were later were analyzed by SEM to understand the effect of laser annealing on the morphology of the nanoparticles. The SEM micrographs were analyzed with the software ImageJ to get information on nanoparticle radius and size distribution and surface covered area.

The experimental results were compared with previously obtained data for thermally annealed samples. It was observed that the spectra of the laser annealed films are not strongly dependent on laser fluence and exhibit spatial variations across the sample surface. Although the overall spectral shape is similar to that of the thermally annealed film, the latter displays a deeper and narrower LSPR dip, which is more suitable for sensing applications. The nanoparticle size histograms revealed that laser annealing produced particles approximately six to seven times larger than those formed by thermal annealing. Furthermore, the broader size distribution observed in the laser-annealed films accounts for the corresponding broadening of the LSPR band compared with the thermally annealed case.

Several numerical simulations were performed to complement and reinforce the insights obtained from the experimental data. By comparing the extinction efficiency of a gold nanosphere fully embedded in a ZnO thin film with that of another completely surrounded by air, we hypothesized that only a fraction

of each nanoparticle must be embedded within the film in order for the LSPR band to be centered around $550\,\mathrm{nm}$, as observed experimentally. To test this hypothesis, a model was developed in which a gold nanosphere in air was coated with a ZnO shell of variable thickness, representing different effective fractions of the nanoparticle volume embedded in the film. The results indicated that approximately 10–20% of the nanoparticle should be embedded to reproduce the experimental resonance position.The temperature evolution of a gold nanosphere was also simulated for two limiting cases: one fully embedded in ZnO and another completely exposed to air. In the first case, the temperature exceeded the melting point of gold, as expected. In the second, it rose well above the boiling point, implying that, if such conditions occurred experimentally, significant material losses could take place. Despite their simplicity, the models and experimental analyses presented in this work provide a coherent qualitative understanding of nanoparticle growth and plasmonic behavior under different annealing conditions. These results should, however, be interpreted with caution, as the models neglect several physical effects and interactions. Nonetheless, they establish a solid conceptual foundation for interpreting the complex mechanisms governing laser-induced nanoparticle heating and morphological evolution. In future work, it would be valuable to acquire SEM images of the samples after different numbers of laser pulses, in order to directly correlate the morphological evolution with the corresponding spectral changes. Additionally, obtaining cross-sectional SEM images of the films would allow visualization of the nanoparticle shape and degree of embedding within the matrix. This information could then be used to refine and improve the numerical simulation models, leading to a more realistic representation of the system. Another promising direction would be to replicate the work of Kalfagiannis et al. [10], but using a gold thin film instead of silver, in order to directly compare the influence of the metal type on the laser-induced self-assembly process. Additionally, laser annealing experiments could be carried out using different laser wavelengths, possibly through the use of an optical parametric amplifier, to evaluate wavelength dependent effects on nanoparticle formation and plasmonic response. It would also be interesting to explore the use of dual wavelength irradiation to investigate potential synergistic effects in nanoparticle growth and reshaping. Another possibility is to vary the fluence of the laser pulses as the nanoparticles grow, which might allow to fine tune the process and obtain a narrower distribution of sizes, which presumably would lead to deeper and narrower LSPR bands.

Bibliography

[1] Peter Vikesland. “Nanosensors for water quality monitoring”. In: *Nature Nanotechnology* 13 (Aug. 2018). DOI: 10.1038/s41565-018-0209-9.

[2] Katherine A. Willets and Richard P. Van Duyne. “Localized Surface Plasmon Resonance Spectroscopy and Sensing”. In: *Annual Review of Physical Chemistry* 58.Volume 58, 2007 (2007), pp. 267–297. ISSN: 1545-1593. DOI: https://doi.org/10.1146/annurev.physchem.58.032806.104607. URL: https://www.annualreviews.org/content/journals/10.1146/annurev.physchem.58.032806.104607.

[3] Marco S. Rodrigues et al. “Gas Sensors Based on Localized Surface Plasmon Resonances: Synthesis of Oxide Films with Embedded Metal Nanoparticles, Theory and Simulation, and Sensitivity Enhancement Strategies”. In: *Applied Sciences* 11.12 (2021). ISSN: 2076-3417. DOI: 10.3390/app11125388. URL: https://www.mdpi.com/2076-3417/11/12/5388.

[4] Siddardha Koneti et al. “Electron Tomography of Plasmonic Au Nanoparticles Dispersed in a TiO2 Dielectric Matrix”. In: *ACS Applied Materials & Interfaces* 10.49 (2018). PMID: 30457319, pp. 42882–42890. DOI: 10.1021/acsami.8b16436. URL: https://doi.org/10.1021/acsami.8b16436.

[5] Diana I. Meira et al. “Enhancing the Extinction Efficiency and Plasmonic Response of Bimetallic Nanoparticles of Au-Ag in Robust Thin Film Sensing Platforms”. In: *Sensors* 23.23 (2023). ISSN: 1424-8220. DOI: 10.3390/s23239618. URL: https://www.mdpi.com/1424-8220/23/23/9618.

[6] Manuela Proença et al. “Nanoplasmonic Au:CuO thin films functionalized with APTES to enhance the sensitivity of gas sensors”. In: *Sensors and Actuators B: Chemical* 401 (2024), p. 134959. ISSN: 0925-4005. DOI: https://doi.org/10.1016/j.snb.2023.134959. URL: https://www.sciencedirect.com/science/article/pii/S0925400523016775.

[7] Patrícia Pereira-Silva et al. “Nanocomposite Au-ZnO thin films: Influence of gold concentration and thermal annealing on the microstructure and plasmonic response”. In: *Surface and Coatings Technology* 385 (2020), p. 125379. ISSN: 0257-8972. DOI: https://doi.org/10.1016/j.surfcoat.2020.125379. URL: https://www.sciencedirect.com/science/article/pii/S0257897220300487.

[8] Diana I. Meira et al. “Label-free localized surface plasmon resonance (LSPR) biosensor, based on Au-Ag NPs embedded in TiO2 matrix, for detection of Ochratoxin-A (OTA) in wine”. In: *Talanta* 284 (2025), p. 127238. ISSN: 0039-9140. DOI: https://doi.org/10.1016/j.talanta.2024.127238. URL: https://www.sciencedirect.com/science/article/pii/S0039914024016175.

[9] Kathryn M. Mayer and Jason H. Hafner. “Localized Surface Plasmon Resonance Sensors”. In: *Chemical Reviews* 111.6 (2011). PMID: 21648956, pp. 3828–3857. DOI: 10.1021/cr100313v. eprint: https://doi.org/10.1021/cr100313v. URL: https://doi.org/10.1021/cr100313v.

[10] Nikolaos Kalfagiannis et al. “Selective modification of nanoparticle arrays by laser-induced self assembly (MONA-LISA): putting control into bottom-up plasmonic nanostructuring”. In: *Nanoscale* 8 (15 2016), pp. 8236–8244. DOI: 10.1039/C5NR09192F. URL: http://dx.doi.org/10.1039/C5NR09192F.

[11] Patrícia Pereira-Silva et al. “Synergistic Effect of ZnO Thin Films with Gold as Antifungal Coatings”. In: *Advanced Engineering Materials* 26.13 (2024), p. 2400342. DOI: https://doi.org/10.1002/adem.202400342. eprint: https://advanced.onlinelibrary.wiley.com/doi/pdf/10.1002/adem.202400342. URL: https://advanced.onlinelibrary.wiley.com/doi/abs/10.1002/adem.202400342.

[12] Michael P. Marder. *Condensed Matter Physics*. John Wiley & Sons, Ltd, 2010. ISBN: 9780470949955. DOI: 10.1002/9780470949955.

[13] Wikipedia contributors. *Charge carrier density — Wikipedia, The Free Encyclopedia*. https://en.wikipedia.org/w/index.php?title=Charge_carrier_density&oldid=1305653040. [Online; accessed 16-October-2025]. 2025.

[14] David Pines. “A Collective Description of Electron Interactions: IV. Electron Interaction in Metals”. In: *Phys. Rev.* 92 (3 Nov. 1953), pp. 626–636. DOI: 10.1103/PhysRev.92.626. URL: https://link.aps.org/doi/10.1103/PhysRev.92.626.

[15] David Pines and David Bohm. “A Collective Description of Electron Interactions: II. Collective vs Individual Particle Aspects of the Interactions”. In: *Phys. Rev.* 85 (2 Jan. 1952), pp. 338–353. DOI: 10.1103/PhysRev.85.338. URL: https://link.aps.org/doi/10.1103/PhysRev.85.338.

[16] Wikimedia Commons. *File:Sketch of surface plasmon.png — Wikimedia Commons, the free media repository*. [Online; accessed 17-October-2025]. 2025. URL: %5Curl%7Bhttps://commons.wikimedia.org/w/index.php?title=File:Sketch_of_surface_plasmon.png&oldid=1007451309%7D.

[17] Olivier Pluchery and Jean-François Bryche. *An Introduction to Plasmonics*. WORLD SCIENTIFIC (EUROPE), 2023. DOI: 10.1142/q0395. eprint: https://www.worldscientific.com/doi/pdf/10.1142/q0395. URL: https://www.worldscientific.com/doi/abs/10.1142/q0395.

[18] Wikimedia Commons. *File:LSPR in gold nanoparticles.jpg — Wikimedia Commons, the free media repository*. [Online; accessed 20-October-2025]. 2024. URL: %5Curl%7Bhttps://commons.wikimedia.org/w/index.php?title=File:LSPR_in_gold_nanoparticles.jpg&oldid=972494096%7D.

[19] Ulrich Hohenester. *Nano and Quantum Optics: An Introduction to Basic Principles and Theory*. Springer Cham, 2020. ISBN: 978-3-030-30503-1. DOI: 10.1007/978-3-030-30504-8.

[20] Donald R. Huffman Craig F. Bohren. “Particles Small Compared with the Wavelength”. In: *Absorption and Scattering of Light by Small Particles*. John Wiley & Sons, Ltd, 1998. Chap. 5, pp. 130–157. ISBN: 9783527618156. DOI: https://doi.org/10.1002/9783527618156.ch5. URL: https://onlinelibrary.wiley.com/doi/abs/10.1002/9783527618156.ch5.

[21] Wikipedia contributors. *Lycurgus Cup — Wikipedia, The Free Encyclopedia*. https://en.wikipedia.org/w/index.php?title=Lycurgus_Cup&oldid=1274151867. [Online; accessed 31-October-2025]. 2025.

[22] Gustav Mie. “Beiträge zur Optik trüber Medien, speziell kolloidaler Metallösungen”. In: *Annalen der Physik* 330.3 (1908), pp. 377–445. DOI: https://doi.org/10.1002/andp.19083300302. URL: https://onlinelibrary.wiley.com/doi/abs/10.1002/andp.19083300302.

[23] Jürgen Waxenegger, Andreas Trügler, and Ulrich Hohenester. "Plasmonics simulations with the MNPBEM toolbox: Consideration of substrates and layer structures". In: *Computer Physics Communications* 193 (2015), pp. 138–150. ISSN: 0010-4655. DOI: https://doi.org/10.1016/j.cpc.2015.03.023. URL: https://www.sciencedirect.com/science/article/pii/S0010465515001228.

[24] Omar Aguilar et al. "Optoelectronic characterization of Zn1-xCdxO thin films as an alternative to photonic crystals in organic solar cells". In: *Opt. Mater. Express* 9.9 (Sept. 2019), pp. 3638–3648. DOI: 10.1364/OME.9.003638. URL: https://opg.optica.org/ome/abstract.cfm?URI=ome-9-9-3638.

[25] George M. Whitesides and Bartosz Grzybowski. "Self-Assembly at All Scales". In: *Science* 295.5564 (2002), pp. 2418–2421. DOI: 10.1126/science.1070821. eprint: https://www.science.org/doi/pdf/10.1126/science.1070821. URL: https://www.science.org/doi/abs/10.1126/science.1070821.

[26] Wikipedia contributors. *Self-assembly of nanoparticles — Wikipedia, The Free Encyclopedia*. https://en.wikipedia.org/w/index.php?title=Self-assembly_of_nanoparticles&oldid=1314733113. [Online; accessed 30-October-2025]. 2025.

[27] J. Borges et al. "Broadband Optical Absorption Caused by the Plasmonic Response of Coalesced Au Nanoparticles Embedded in a TiO2 Matrix". In: *The Journal of Physical Chemistry C* 120.30 (2016), pp. 16931–16945. DOI: 10.1021/acs.jpcc.6b03684. URL: https://doi.org/10.1021/acs.jpcc.6b03684.

[28] Diana I. Meira et al. "Enhancing the Extinction Efficiency and Plasmonic Response of Bimetallic Nanoparticles of Au-Ag in Robust Thin Film Sensing Platforms". In: *Sensors* 23.23 (2023). ISSN: 1424-8220. DOI: 10.3390/s23239618. URL: https://www.mdpi.com/1424-8220/23/23/9618.

[29] Guillaume Baffou. *Thermoplasmonics: Heating Metal Nanoparticles Using Light*. Cambridge University Press, 2017.

[30] Khaled Metwally, Serge Mensah, and Guillaume Baffou. "Fluence Threshold for Photothermal Bubble Generation Using Plasmonic Nanoparticles". In: *The Journal of Physical Chemistry C* 119.51 (2015), pp. 28586–28596. DOI: 10.1021/acs.jpcc.5b09903. eprint: https://doi.org/10.1021/acs.jpcc.5b09903. URL: https://doi.org/10.1021/acs.jpcc.5b09903.

[31] Guillaume Baffou and Hervé Rigneault. "Femtosecond-pulsed optical heating of gold nanoparticles". In: *Phys. Rev. B* 84 (3 July 2011), p. 035415. DOI: 10.1103/PhysRevB.84.035415. URL: https://link.aps.org/doi/10.1103/PhysRevB.84.035415.

[32] Thorlabs. [Online; accessed 25-October-2025]. URL: %5Curl%7Bhttps://www.thorlabs.com/thorproduct.cfm?partnumber=MNWHL4%7D.

[33] G.D. Danilatos. "Theory of the Gaseous Detector Device in the Environmental Scanning Electron Microscope". In: ed. by Peter W. Hawkes. Vol. 78. Advances in Electronics and Electron Physics. Academic Press, 1990, pp. 1–102. DOI: https://doi.org/10.1016/S0065-2539(08)60388-1. URL: https://www.sciencedirect.com/science/article/pii/S0065253908603881.

[34] Joseph I. Goldstein et al. *Scanning Electron Microscopy and X-Ray Microanalysis*. 4th. Springer New York, 2018. ISBN: 978-1-4939-6674-5. DOI: https://doi.org/10.1007/978-1-4939-6676-9.

[35] Ilia L. Rasskazov, P. Scott Carney, and Alexander Moroz. “STRATIFY: a comprehensive and versatile MATLAB code for a multilayered sphere”. In: *OSA Continuum* 3.8 (Aug. 2020), pp. 2290–2306. DOI: 10.1364/OSAC.399979. URL: https://opg.optica.org/osac/abstract.cfm?URI=osac-3-8-2290.